

1 **Inclusion of mountain wave-induced cooling for the**  
2 **formation of PSCs over the Antarctic Peninsula in a**  
3 **chemistry-climate model**

4  
5 **A. Orr<sup>1</sup>, J. S. Hosking<sup>1</sup>, L. Hoffmann<sup>2</sup>, J. Keeble<sup>3</sup>, S. M. Dean<sup>4</sup>, H. K. Roscoe<sup>1</sup>, N.**  
6 **L. Abraham<sup>5,3</sup>, S. Vosper<sup>6</sup>, and P. Braesicke<sup>7</sup>**

7  
8 [1]{British Antarctic Survey, NERC, Cambridge, United Kingdom}

9 [2]{Jülich Supercomputing Centre, Forschungszentrum Jülich, Jülich, Germany}

10 [3]{University of Cambridge, Cambridge, United Kingdom}

11 [4]{National Institute of Water and Atmospheric Research, Auckland, New Zealand}

12 [5]{National Centre for Atmospheric Science, United Kingdom}

13 [6]{Met Office, Exeter, United Kingdom}

14 [7]{Karlsruhe Institute of Technology, Karlsruhe, Germany}

15  
16 Correspondence to: A. Orr (anmcr@bas.ac.uk)

17  
18 To be submitted to: *Atmospheric Chemistry and Physics*

19  
20 May 2014

21  
22 **Abstract**

23 An important source of polar stratospheric clouds (PSCs), which play a crucial role in  
24 controlling polar stratospheric ozone depletion, is from the temperature fluctuations induced  
25 by mountain waves. However, this formation mechanism is usually missing in chemistry-  
26 climate models because these temperature fluctuations are neither resolved nor parameterised.

1 Here, we investigate the representation of stratospheric mountain wave-induced temperature  
2 fluctuations by the UK Met Office Unified Model (UM) at high and low spatial resolution  
3 against Atmospheric Infrared Sounder satellite observations for three case studies over the  
4 Antarctic Peninsula. At a high horizontal resolution (4 km) the mesoscale configuration of  
5 the UM correctly simulates the magnitude, timing, and location of the measured temperature  
6 fluctuations. By comparison, at a low horizontal resolution ( $2.5^\circ \times 3.75^\circ$ ) the climate  
7 configuration fails to resolve such disturbances. However, it is demonstrated that the  
8 temperature fluctuations computed by a mountain wave parameterisation scheme inserted into  
9 the climate configuration (which computes the temperature fluctuations due to unresolved  
10 mountain waves) are in excellent agreement with the mesoscale configuration responses. The  
11 parameterisation was subsequently used to compute the local mountain wave-induced cooling  
12 phases in the chemistry-climate configuration of the UM. This increased stratospheric  
13 cooling was passed to the PSC scheme of the chemistry-climate model, and caused a 30-50%  
14 increase in PSC surface area density over the Antarctic Peninsula compared to a 30-year  
15 control simulation.

16

## 17 **1 Introduction**

18 Gravity waves generated by stratified flow passing over orography (mountain waves) that  
19 propagate into the stratosphere play a crucial role in the formation of polar stratospheric  
20 clouds (PSCs). Adiabatic temperature changes resulting from mountain wave-induced  
21 vertical displacement can drive significant localised temperature fluctuations, enabling  
22 stratospheric temperatures to fall below the threshold value for PSC formation in the cold  
23 phases of these waves even if the synoptic-scale temperatures are too high. Studies of  
24 individual cases show that mountain waves formed over regions including the Antarctic  
25 Peninsula, Greenland, and northern Scandinavia are a significant source of such clouds by  
26 generating localised cooling of up to  $\sim 15$  K (e.g. Carslaw et al., 1998a; Dörnbrack et al.,  
27 1999, 2002, 2012; Noel et al., 2009).

28 The threshold temperatures for PSC formation at an altitude of around 20 km depend on  
29 composition (in particular water vapour and nitric acid) and are generally assumed to be 195  
30 K for type Ia (nitric acid trihydrate particles), 191 K for type Ib (supercooled ternary solution  
31 droplets), and 188 K for type II (water ice particles) (Pawson et al., 1995; Alfred et al., 2007).  
32 Within the centre of the Antarctic stratospheric vortex in winter, the atmosphere is so cold

1 that temperatures are regularly below these thresholds, i.e. formation of PSCs on the synoptic-  
2 scale dominates (Campbell and Sassen, 2008). Despite this, mountain waves are an important  
3 source of PSCs above e.g. the Antarctic Peninsula in the earlier and later stages of winter  
4 when synoptic-scale temperatures can be warmer than the formation thresholds (McDonald et  
5 al., 2009; Noel and Pitts, 2012). By contrast, because of stronger planetary wave forcing, the  
6 Arctic stratospheric vortex is generally considerably warmer than that of the Antarctic. Thus,  
7 the occurrence of PSC formation temperatures on the synoptic-scale is less frequent in the  
8 Arctic (Pawson et al., 1995), thereby making mountain wave-induced PSCs an important  
9 source (Dörnbrack et al., 2001; Alexander et al., 2013). Moreover, mountain waves are a  
10 significant source of PSCs on the synoptic-scale in both the Arctic and Antarctic due to their  
11 advection far downstream of the wave event that formed them (Carslaw et al., 1999; Höpfner  
12 et al., 2006; Eckermann et al., 2009; Alexander et al., 2011).

13 The role of PSC particles in polar ozone chemistry is generally well understood. The  
14 conversion of passive species of chlorine and bromine to active forms that destroy  
15 stratospheric ozone in sunlight takes place on the surface of PSCs (Solomon, 1999).  
16 Furthermore, the removal of nitric acid from the atmosphere by sedimentation of PSC  
17 particles leads to a slower conversion of active chlorine back into its passive species (Jensen  
18 et al., 2002). The Antarctic ozone hole has profound impacts on the Southern Hemisphere  
19 circulation and surface climate during summer (e.g. Orr et al., 2008, 2012; Thompson et al.,  
20 2011). With the continued implementation of the Montreal Protocol, recovery of the Antarctic  
21 ozone hole is generally anticipated by the end of the century. However, model predictions  
22 using coupled chemistry-climate simulations give a large range of estimates of the rate and  
23 timing of this recovery (Eyring et al., 2013). The fact that the results are model dependent  
24 suggests that some mechanisms are not yet fully understood. Similarly, simulations of the  
25 ozone hole covering the past few decades obtain a wide range of results, further questioning  
26 the value of these predictions (Austin et al., 2010). Accurate predictions of the timing are  
27 critical as this recovery will reshape Southern Hemisphere climate by no-longer counteracting  
28 the effects of increasing greenhouse gases (Polvani et al., 2011).

29 Therefore, to produce accurate simulations of stratospheric ozone depletion, coupled  
30 chemistry-climate models must be able to represent PSC formation mechanisms and their  
31 attendant ozone-loss chemistry due to localised dynamics such as mountain waves (Cariolle et  
32 al., 1989; Carslaw et al., 1998b; Austin et al., 2010). However, current chemistry-climate

1 models have a spatial resolution of some hundreds of kilometres (e.g. Morgenstern et al.,  
2 2010) at the equator and are therefore only able to explicitly resolve waves with long  
3 horizontal wavelengths (Reinecke and Durran, 2009), i.e. the temperature fluctuations  
4 associated with small-scale mountain waves are missing, leading to insufficient PSC  
5 formation in the models. Consistent with this is the systematic over-prediction of high-  
6 latitude spring time ozone increases in both hemispheres by models (Carslaw et al. 1998b,  
7 Eyring et al. 2006).

8 Mountain wave-induced stratospheric temperature fluctuations can be detected by their  
9 associated fluctuations in temperature-sensitive satellite radiance measurements from infrared  
10 scanning instruments such as the Atmospheric Infrared Sounder (AIRS) (e.g. Alexander and  
11 Barnett, 2007; Hoffmann et al., 2013). As a nadir viewing instrument, AIRS radiance  
12 measurements have a high horizontal resolution (14 km at nadir), enabling waves with short  
13 horizontal scales which are unresolved by chemistry-climate models to be visible. On the  
14 other hand, AIRS radiance measurements have a limited vertical resolution, meaning waves  
15 with short (typically  $\leq 10$  km) vertical scales are poorly resolved. Comparison between AIRS  
16 radiance measurements and model simulated radiance measurements (calculated using the  
17 simulated temperature field of the model as input for a radiative transfer model) provides an  
18 effective and direct means of validation of the model representation of gravity wave events  
19 (Grimsdell et al., 2010).

20 To improve the simulation of mountain wave-induced PSCs in a chemistry-climate model, the  
21 temperature fluctuations due to unresolved (sub-grid scale) mountain waves can be  
22 parameterised (e.g. Carslaw et al., 1999; Dean et al., 2007; Wells et al., 2011). In the  
23 parameterisation scheme of Dean et al. (2007) the mountain wave-induced temperature  
24 fluctuations were used in the cloud scheme of the HadAM3 (Hadley Centre Atmospheric  
25 Model version 3) configuration of the Met Office Unified Model (UM) to realistically  
26 represent cirrus in the upper-troposphere, which was previously under-represented over many  
27 mountain ranges. In this study, the Dean et al. (2007) scheme is used to improve the  
28 simulation of mountain wave-induced PSCs in the United Kingdom Chemistry and Aerosol  
29 (UKCA) module, which is the chemistry-climate configuration of the UM (section 5). Our  
30 approach firstly requires demonstration of the ability of the parameterisation to reasonably  
31 simulate stratospheric temperature fluctuations. This is achieved by using case studies of  
32 AIRS measurements to validate high resolution simulations (using the mesoscale

1 configuration of the UM) of mountain wave-induced stratospheric temperature fluctuations  
2 above the Antarctic Peninsula (section 3). The Antarctic Peninsula is chosen because strong  
3 westerly winds impinging on its high topographic ridge frequently generate large-amplitude  
4 stratospheric mountain waves (Plougonven et al., 2008; Hoffmann et al., 2013) with  
5 horizontal wavelengths of  $\sim 300$  km (as well as structures on shorter horizontal scales) and  
6 long ( $\geq 10$  km) vertical wavelengths (Wu, 2004; Alexander and Teitelbaum, 2007), i.e.  
7 resolved by AIRS. The long vertical wavelengths result from wave refraction caused when  
8 the background wind speed is unidirectional and increases with height (see e.g. Wu and  
9 Eckermann, 2008). Following this, the Dean et al. (2007) scheme is inserted into the climate  
10 configuration of the UM and its temperature fluctuations are assessed by comparing with  
11 output from the high resolution simulations (section 4). We will demonstrate below that the  
12 high resolution simulations are in excellent agreement with the AIRS observations, and can  
13 therefore be used as a ‘truth’ with which to investigate the performance of the  
14 parameterisation scheme. The paper finishes with a summary and discussion (section 6).

15

## 16 **2 Models, mountain wave parameterisation, data, and methodology**

### 17 **2.1 Models**

18 The UM is a numerical modelling system based on non-hydrostatic dynamics which can be  
19 run with varying configurations, including for this study as a mesoscale model, a climate  
20 model, and a chemistry-climate model. The climate model is based on the HadGEM3  
21 (Hadley Centre Global Environmental Model version 3) configuration of the UM (Hewitt et  
22 al., 2011). The UKCA chemistry-climate model (Morgenstern et al., 2009) runs within the  
23 UM climate configuration. UKCA uses a simple scheme for calculating the presence of PSC  
24 particles, based on the assumption that they are in thermodynamic equilibrium with the gas  
25 phase (e.g. Feng et al., 2011). Here, both the climate and chemistry-climate configurations  
26 are atmosphere-only models based on version 7.3 of the UM, with a horizontal resolution of  
27 N48 ( $96 \times 73$  grid points, or  $2.5^\circ \times 3.75^\circ$ ) and 60 vertical levels (going up to 84 km). Version  
28 7.3 of the UM was selected for the global modelling exercise because of its current use in a  
29 recent, comprehensive model intercomparison (SPARC Report N°6, 2013).

30 The mesoscale model is based on version 7.6 of the UM, and is similar to that described in  
31 Orr et al. (2014). It is atmosphere-only with a model domain centered over the Antarctic

1 Peninsula, comprising  $388 \times 460$  grid points with a horizontal resolution of 4 km and 85  
2 vertical levels (going up to 85 km). Following Webster et al. (2008), it uses the option of a  
3 fully three-dimensional potential temperature advection scheme, in conjunction with reduced  
4 temporal off-centering, to better represent resolved gravity waves. Orography is interpolated  
5 from a high-resolution digital elevation model of Antarctica (version 9 of the Radarsat  
6 Antarctic Mapping Project, Liu et al. 2001). The mesoscale model is nested within a coarser  
7 resolution UM global model at a horizontal resolution of N512 ( $1024 \times 769$  grid points, or  
8  $0.352^\circ \times 0.234^\circ$ ) and 70 vertical levels (going up to 80 km), i.e. output from global model  
9 forecasts (excluding sea ice state and sea surface temperature) are used as initialisation and  
10 boundary values. Initialisation values for sea ice state and sea surface temperature for the  
11 mesoscale model were obtained from high-resolution ( $\sim 5$  km scale) daily Operational Sea  
12 Surface Temperature and Sea Ice Analysis (OSTIA) data (Donlon et al. 2011). The Met  
13 Office operational analysis is used to initialise the global model. Version 7.6 of the UM was  
14 selected for the mesoscale model as it included improvements which reduced the occurrence  
15 of spurious cooling in partially resolved valleys.

## 16 **2.2 Description of the mountain wave parameterisation**

17 By assuming that waves are forced by steady flow over a two-dimensional ridge and that  
18 vertical variations of the background atmospheric state are slowly varying (compared to the  
19 wave phase), the scheme described by Dean et al. (2007) derives generalised expressions for  
20 the maximum and minimum vertical streamline displacement (resulting in cooling and  
21 warming, respectively) associated with gravity waves induced by sub-grid scale orography  
22 (SSO). These expressions are used to compute the maximum negative  $\Delta T_{SSO}^-$  and positive  
23  $\Delta T_{SSO}^+$  temperature fluctuations associated with the displacement, which are derived using the  
24 local potential temperature gradient (Wells et al., 2011). The overall temperature fluctuation  
25 induced is subsequently calculated as  $\Delta T_{SSO} = \Delta T_{SSO}^+ + \Delta T_{SSO}^-$ . Waves are launched at every  
26 model grid box over land and at every model time step.

27 The expressions for the maximum and minimum streamline displacement depend on both the  
28 wave phase and peak vertical streamline displacement amplitude (hereafter referred to as  
29 wave amplitude), which are determined as follows. The vertical propagation is based on  
30 linear theory for hydrostatic waves forced by steady, stably stratified flow over a two-  
31 dimensional ridge, assuming that vertical variations of the background atmospheric state are

1 slowly varying. McFarlane (1987) showed that under these circumstances and in the absence  
2 of dissipation mechanisms that the vertical evolution of the wave amplitude is determined by  
3 the decrease in density of the atmosphere with height and by changes in the horizontal wind  
4 speed  $U$  (resolved in the direction of the wave vector) and the Brunt-Väisälä frequency  $N$ .  
5 Dissipation mechanisms such as wave-breaking and critical level absorption are introduced by  
6 preventing the amplitude from exceeding the local ‘saturation amplitude’ for which the wave  
7 field becomes unstable ( $= U / NF_{sat}$ , where  $F_{sat}$  is the critical Froude number for saturation).  
8 The vertical evolution of the wave phase is determined by changes in  $U$  and  $N$ , i.e. the Scorer  
9 parameter  $l(\approx N / U)$ .

10 To complete the determination of the wave phase and amplitude, their initial values at the top  
11 of the blocked layer must be decided. The initial wave phase is set equal to zero. The initial  
12 wave amplitude is set equal to the ‘effective’ mountain height  $h_{eff}$  ( $= h - h_b$ , where  $h$  is the  
13 height of the sub-grid scale mountain and  $h_b$  is the height of the blocked layer that occurs at  
14 low Froude number), i.e. the maximum vertical displacement of streamlines able to pass over  
15 the top of the mountain. This is strongly dependent on the direction of the low-level wind  
16 relative to the principle axis of the SSO (which preferentially aligns as ridges), and ensures  
17 that the surface amplitude is large (small) when the wind is perpendicular (parallel) to a ridge.  
18 Here,  $h = n_\sigma \sigma$ , where  $\sigma$  is the standard deviation of the SSO height from the grid-box mean  
19 and  $n_\sigma$  is a constant (such that  $n_\sigma \sigma$  approximates the physical envelope of the peaks), and  
20  $h_b = h - U_0 / N_0 F_c$ , where  $F_c$  is the critical Froude number at which flow blocking is deemed  
21 to first occur, and the subscript ‘0’ refers to the surface layer, represented by averaging  $U$  and  
22  $N$  between the surface and  $h$ . Note that to implement the directional dependence of the  
23 surface amplitude,  $U_0$  is resolved in the direction perpendicular to the principle axis of the  
24 sub-grid orography (i.e. the direction of the wave vector). This differs from the  
25 implementation in Dean et al. (2007) which represents the directional dependence by defining  
26 the standard deviation  $\sigma$  of the SSO height in the surface wind direction.

27 The parameterisation scheme is implemented in the climate and chemistry-climate  
28 configurations of the UM. The SSO parameters used by the scheme are based on Lott and  
29 Miller (1997). In the scheme the parameters  $n_\sigma$ ,  $F_{sat}$  and  $F_c$  are treated as tuneable.  
30 Following an initial sensitivity study to optimise the performance of the scheme (not shown),  
31 their values were set to  $n_\sigma = 3$ ,  $F_{sat} = 2$  and  $F_c = 4$ .

## 1 **2.3 Data**

2 AIRS (Aumann et al., 2003) is aboard the National Aeronautics and Space Administration's  
3 Aqua satellite, which was launched in May 2002. AIRS measures the thermal emissions of  
4 atmospheric constituents in the nadir and sub-limb observation geometry. An across-track  
5 scan consists of 90 individual footprints and covers a distance of 1765 km on the ground. The  
6 along-track distance between two scans is 18 km. The AIRS aperture is  $1.1^\circ$ , corresponding to  
7 a spatial resolution of 13.5 km at nadir and  $41 \text{ km} \times 21.4 \text{ km}$  at the scan extremes. The AIRS  
8 radiance measurements cover wavelength ranges from 3.74 to 15.4  $\mu\text{m}$  with a total of 2378  
9 radiance channels. The absolute error of the radiometric calibration is less than 0.2%. The  
10 noise equivalent delta temperature is about 0.39 K at 250 K scene temperature for the spectral  
11 channel ( $666.5 \text{ cm}^{-1}$ ) considered here. The analyses presented in this paper are based on  
12 consolidated version 5 data products made freely available by NASA. The equatorial crossing  
13 of Aqua occurs at 13:30 local time (ascending orbit) and 01:30 local time (descending orbit).  
14 At high latitudes there is a quick transition between day- and night-time observations (e.g.,  
15 Hoffmann et al., 2013). The Antarctic Peninsula is typically covered by four satellite  
16 overpasses per day. A more detailed description of AIRS is given in e.g. Hoffmann and  
17 Alexander (2009, 2010), Grimsdell et al. (2010), or Hoffmann et al. (2013).

18 Infrared radiance measurements in the 4.3 and 15  $\mu\text{m}$   $\text{CO}_2$  bands are of particular interest for  
19 the study of stratospheric gravity waves. These bands get optically thick in the stratosphere  
20 and as the  $\text{CO}_2$  concentration does not vary substantially in the lower and middle atmosphere,  
21 the radiance measurements in these channels are most sensitive to atmospheric temperature.  
22 Hoffmann and Alexander (2009) show the temperature kernel functions for the individual  
23 AIRS channels covering the 4.3 and 15  $\mu\text{m}$   $\text{CO}_2$  bands. In this study we selected the  $666.5$   
24  $\text{cm}^{-1}$  radiance channel of AIRS, which is within the 15  $\mu\text{m}$   $\text{CO}_2$  band. The temperature  
25 weighting function of this channel is given in Fig. 1, which shows that the brightness  
26 temperatures  $BT$  are most sensitive to atmospheric temperature at an altitude of 22 km, with  
27 full width at half maximum of 9 km. The altitude range covered by the  $666.5 \text{ cm}^{-1}$  channel is  
28 of particular interest for the formation of PSCs. As the kernel function drops to less than 1%  
29 of maximum sensitivity below 14 km, there is little interference from tropospheric emissions  
30 from clouds or water vapour.



## 1 **2.4 Methodology**

2 Three instances of stratospheric mountain waves observed over the Antarctic Peninsula by  
3 AIRS, characterised by large amplitude and long vertical wavelength, occurred on 7 August  
4 2011 at 03:40 UTC (case study 1, hereafter CS1), 2 August 2010 at 18:59 UTC (case study 2,  
5 hereafter CS2), and 14 July 2010 at 20:00 UTC (case study 3, hereafter CS3). These events  
6 were simulated by running the mesoscale model for a 48 hour period driven by output from  
7 global model forecasts (following a 3 hour spin-up) initialised on 5 August 2011 at 12:00  
8 UTC for CS1, 1 August 2010 at 00:00 UTC for CS2, and 13 July 2010 at 00:00 UTC for CS3.  
9 The mesoscale model output times (integration time) closest to the actual measurement time  
10 are at 03:00 UTC on 7 August 2011 (T+39 h) for CS1, at 19:00 UT on 2 August 2010 (T+43  
11 h) for CS2, and at 20:00 UT on 14 July 2010 (T+44 h) for CS3 (note that for simplicity the  
12 mesoscale model integration times are given relative to the time of the global model  
13 initialisation). The output times reflect that the simulation of the mountain wave field  
14 requires at least a 24 hour spin-up (Plougonven et al., 2010). Table 1 summarises this  
15 information. Fig. 2 shows the near-surface (850 hPa) wind field simulated by the mesoscale  
16 model at the output time for each case study, showing that each of the mountain wave events  
17 were coincident with strong westerly or north-westerly winds incident to the peninsula. These  
18 winds showed the requisite strengthening with height required for the mountain waves to have  
19 long vertical wavelengths which were visible to AIRS (not shown).

20 To verify the mesoscale model forecasts the Juelich Rapid Spectral Simulation Code  
21 (JURASSIC) radiative transfer model (Hoffmann and Alexander, 2009) was used to compute  
22 model simulated AIRS radiances at  $666.5 \text{ cm}^{-1}$ . For comparison, both the real and mesoscale  
23 model simulated AIRS radiances are subsequently converted into their corresponding  $BT$   
24 values. Brightness temperature perturbations  $\Delta BT$  were computed by removing a  
25 background brightness temperature, which was determined by fitting a 4th-order polynomial  
26 (e.g. Wu, 2004; Alexander and Barnett, 2007; Hoffmann and Alexander, 2010). This fit  
27 removes slowly varying atmospheric signals, e.g. from planetary waves and general scan-  
28 angle dependence of radiances due to the sub-limb geometry. For the AIRS measured  
29 radiances the fit was carried out for each scan in the across-track direction; for the mesoscale  
30 model simulated radiances it was carried out for each latitudinal band of the model grid. In  
31 both cases it was found that the fits are well constrained by the data and the process did not  
32 introduce any artificial wave-like structures that could obfuscate the results. In order to avoid

1 the suppression of waves with fronts parallel to the fit direction the AIRS measured  
2 (simulated) background estimates were smoothed by a 300 km running mean in the along-  
3 track (longitudinal) direction. Finally, mesoscale model estimates of  $\Delta BT$  are re-gridded to  
4 the AIRS measurement grid.

5 The mesoscale model forecasts were repeated using the climate model (i.e. the climate model  
6 is initialised using the same Met Office operational analysis and integrated forward in time for  
7 48 hours). Comparison of the mesoscale model and climate model simulations of the near-  
8 surface winds at the time of the mountain wave events (Fig. 2) shows relatively small  
9 differences in the large-scale flow impacting the peninsula, i.e. the large-scale atmospheric  
10 conditions responsible for the initial forcing of the mountain waves are broadly similar in both  
11 models. As the mountain wave parameterisation scheme is implemented in the climate  
12 model, the temperature fluctuations predicted by the scheme  $\Delta T_{SSO}$ , as well as the  
13 temperature fluctuations explicitly resolved by the climate model  $\Delta T_{CLM}$  (computed by  
14 removing the background temperature, determined by fitting a 4th-order polynomial), can be  
15 assessed by comparing with those from the mesoscale model. Using the mesoscale model  
16 simulations enables investigation of the vertical profile of the parameterised output, in  
17 particular the vertical evolution of the wave phase, which is not possible at good vertical  
18 resolution using AIRS data alone. In the climate model implementation,  $\Delta T_{SSO}$  is passed  
19 solely to the model output to enable its evaluation and is not used by the dynamical core or  
20 any other parameterisation scheme.

21 Finally, to assess the impact of the scheme on PSC microphysics and chemistry, perturbation  
22 and control experiments using the chemistry-climate model were conducted. In the  
23 perturbation experiments the mountain wave parameterisation is switched on. Following  
24 Carslaw et al. (1999), only the cooling phase  $\Delta T_{SSO}^-$  of the parameterised temperature  
25 fluctuations are coupled to the PSC scheme, meaning that the warm phase is neglected.  
26 Carslaw et al. (1999) argue that this approach is physically justified as the warming phase of  
27 the wave-induced temperature fluctuations is typically of short enough duration that the  
28 complete evaporation of the PSC particles is unlikely to occur before temperatures fall again.  
29 In addition, evaporation will not occur if the synoptic-scale temperatures are sufficiently low  
30 that the warming phase still results in the temperature being below the PSC threshold value.  
31 The PSC scheme computes a ‘total’ temperature, used only by itself, by combining the

1 temperature explicitly resolved by the chemistry-climate model  $T_{CHEM-CLIM}$  with  $\Delta T_{SSO}^-$ . In  
2 the control experiment the mountain wave scheme is switched off. Both the perturbation and  
3 control experiments were run for 30 years (following a 30 year spin-up period) for a perpetual  
4 year-2000, using prescribed sea-surface temperatures and sea ice concentrations.

5

### 6 **3 Mesoscale model verification**

7 Figure 3 compares maps of measured and mesoscale model simulated estimates of  $\Delta BT$  for  
8 each of the three case studies. In the left panels the measured field  $\Delta BT_{AIRS}$  shows warm and  
9 cold temperature disturbances of amplitude 2-3 K clearly aligned with the western side of the  
10 peninsula mountain ridge, i.e. typical of phase fronts associated with a mountain wave caused  
11 by low-level westerly flow passing over the peninsula and propagating upward in the  
12 atmosphere. In the right panels the amplitude and structure of the corresponding mesoscale  
13 model field  $\Delta BT_{MES}$  agrees well with the measurements.

14 Figure 4 compares  $\Delta BT_{AIRS}$  and  $\Delta BT_{MES}$  in more detail by examining their variation along the  
15 west-east orientated lines displayed in Fig. 3. The mountain wave appears prominently in  
16 both fields, with the mesoscale model producing a similar looking temperature disturbance to  
17 that measured. There are slight differences in terms of the wave amplitude, e.g. the mesoscale  
18 model amplitude in CS3 is slightly larger than that measured.

19 Note that in addition to a coherent mountain wave structure, Figs. 3 and 4 also show highly  
20 localised temperature fluctuations. For AIRS these fluctuations are partly due to increasing  
21 instrumental noise with low scene temperatures. The nominal noise of 0.39 K at 250 K scene  
22 temperature scales to 0.67 – 0.78 K at 190 – 200 K, which is more representative for the  
23 situations observed here.

24

### 25 **4 Assessment of the mountain wave parameterisation**

26 Having shown a very good comparison between measured and mesoscale model simulated  
27  $\Delta BT$  in the last section, we can now use the temperature fluctuations simulated by the  
28 mesoscale model  $\Delta T_{MES}$  to assess the parameterised temperature fluctuations  $\Delta T_{SSO}$ , as well  
29 as the temperature fluctuations explicitly resolved by the climate model  $\Delta T_{CLIM}$ . However,

1 due to the occurrence of spatially highly localised and strongly varying temperature  
2 fluctuations, the fairest approach is to compare profiles of  $\Delta T_{SSO}$  and  $\Delta T_{CLIM}$  for a particular  
3 N48 grid box with the mean and spread ( $\pm$  two standard deviations) of  $\Delta T_{MES}$  for all the  
4 mesoscale model points within the same N48 grid box. This is shown in Fig. 5 for the N48  
5 grid box centered at  $-70^\circ$  latitude and  $-63.75^\circ$  longitude, i.e. over the high-level ridge of the  
6 Antarctic Peninsula. The comparison shows that  $\Delta T_{SSO}$  and the mean  $\Delta T_{MES}$  response are  
7 generally in excellent agreement in terms of amplitude (which ranges from 5 to 10 K in the  
8 lower stratosphere), while  $\Delta T_{SSO}$  and the mean  $\Delta T_{MES}$  response are slightly out of alignment in  
9 terms of phase, evident by the maximum and minimum values of  $\Delta T_{SSO}$  being roughly 1 km  
10 lower than those of the mean  $\Delta T_{MES}$  response. However, at all altitudes  $\Delta T_{SSO}$  lies within the  
11 spread of  $\Delta T_{MES}$  (which reaches  $\pm 15$  K in the lower stratosphere), suggesting that the  
12 parameterised temperature fluctuations are representative of the range of mesoscale model  
13 responses. Furthermore, the comparison shows that  $\Delta T_{CLIM}$  completely fails to represent any  
14 temperature fluctuations, i.e. confirmation that the horizontal scale of the mountain waves are  
15 too small to be resolved by climate models, and hence their effects must be parameterised.  
16 Note that additional climate model runs at N96 resolution ( $192 \times 145$  grid points, or  $1.875^\circ \times$   
17  $1.25^\circ$ ) also completely failed to resolve any temperature fluctuations (not shown).

18 Figure 6 compares  $\Delta T_{MES}$  and  $\Delta T_{SSO}$  along a west-east cross section intersecting the Peninsula  
19 at  $-70^\circ$  latitude. Only results for CS3 are shown as those for CS1 and CS2 were largely  
20 similar. The predominant feature of the  $\Delta T_{MES}$  response is, as expected, a large-amplitude,  
21 vertically propagating mountain wave with phase lines tilting upstream with height,  
22 characterised by a horizontal wavelength of around 200 km, a vertical wavelength of around  
23 15 km, and a amplitude of up to 15 K (in the lower stratosphere). It is clearly apparent that  
24 although the parameterisation scheme qualitatively captures the mesoscale model estimate of  
25 the temperature fluctuations in the lower stratosphere directly above the Peninsula, it: i) fails  
26 to capture the upstream tilt of the phase lines, i.e. its phase lines are horizontal and do not tilt  
27 with height, and ii) significantly underestimates the amplitude of the temperature fluctuations.  
28 The lack of phase tilt is due to the parameterised wave field being represented by a  
29 hydrostatic gravity wave launched from an isolated bell-shaped ridge for each grid-box,  
30 which is then only propagated vertically through the column of air above. This simplification

1 is also prohibitive in modelling the full downstream response. At N48 resolution the Antarctic  
 2 Peninsula is multiple grid boxes wide as its resolved orography field is hugely  
 3 smoothed/flattened (see Fig. 6) and is thus represented in the parameterisation as a series of  
 4 very similar sub-grid ridges, while in the mesoscale model the Peninsula is resolved as a  
 5 dominant wide single ridge. Therefore the parameterisation produces a simplified broad  
 6 response, which has smaller amplitude compared to the mesoscale model, across the  
 7 Peninsula, whereby any change in phase can only result from changes in  $U$  and  $N$  within each  
 8 vertical column across the Peninsula. Further comparison of the mesoscale model and climate  
 9 model simulations in Figs 7 and 8 shows that with one exception (the lower altitude part of  
 10 CS1) that  $U$  and  $N$  simulated by the climate model lie within the spread of the mesoscale  
 11 model responses, i.e. indicating that the large-scale atmospheric conditions responsible for the  
 12 parameterised phase evolution are representative of the range of mesoscale model responses.  
 13 Furthermore, given its broad-scale response, it cannot be expected that the parameterised  
 14 temperature fluctuations match the amplitude of the fine-scale fluctuations simulated by the  
 15 mesoscale model. If the mesoscale model response would be spatially averaged the  
 16 amplitudes would be in good agreement.

17

## 18 **5 Impact of the mountain wave parameterisation on PSC formation**

19 Having shown that the parameterised mountain wave-induced temperature fluctuations are  
 20 broadly consistent with the mesoscale model results, we can progress to assessing the impact  
 21 of including the wave-induced cooling phase  $\Delta T_{SSO}^-$  in the chemistry-climate model, again  
 22 concentrating on the Antarctic Peninsula. In the first instance, we will examine the impact on  
 23 the temperatures seen by the PSC scheme. Fig. 9 shows for July at a height of 21 km the 30-  
 24 year average difference in the frequency  $f$  of the temperature falling below the 195 K and  
 25 188 K thresholds for PSC formation of type Ia and II, respectively. The differences are  
 26 between the frequency based on the explicitly resolved temperature  $T_{CHEM-CLIM}$  plus  $\Delta T_{SSO}^-$   
 27 from the perturbation run, and the frequency based solely on the explicitly resolved  
 28 temperature of the perturbation run, i.e.  $f_{T_{CHEM-CLIM} + \Delta T_{SSO}^-} - f_{T_{CHEM-CLIM}}$ . The differences in  
 29 frequency are always positive, which is consistent with only mountain wave cooling being  
 30 used. The results show that over much of the Peninsula, the impact of the mountain wave  
 31 cooling is to increase the frequency that the 195 K threshold is exceeded, peaking over its

1 northern tip with a frequency difference of 4 percentage points. By comparison, the impact  
2 on the 188 K temperature threshold is even more dramatic, resulting in differences which are  
3 both larger and extending much further south, peaking over Alexander Island to the south-  
4 west of the Peninsula with a frequency difference of over 6 percentage points. The fact that  
5 the differences in 195 K threshold frequency are located predominately over the middle and  
6 northern sections of the Peninsula is consistent with the climatological 195 K isotherm of the  
7 perturbation run being situated at approximately  $-75^\circ$  latitude (not shown). Hence, any  
8 increase in the frequency of temperatures falling below 195 K as a result of the  
9 parameterisation can only occur northward of this, i.e. where the large-scale temperature is  
10 not already less than 195 K. Similarly, the differences in 188 K threshold frequency which  
11 encompass the entire length of the Peninsula are consistent with the model 188 K isotherm  
12 being situated southward of the 195 K isotherm (not shown). Fig. 10 compares the 30-year  
13 temperature distribution based on  $T_{CHEM-CLIM} + \Delta T_{SSO}^-$  of the perturbation run against that of  
14  $T_{CHEM-CLIM}$  for the perturbation run for the same N48 grid box used for Figs. 5, 7 and 8, again  
15 for July and at 21 km. As expected, inclusion of the parameterised mountain wave cooling  
16 shifts the temperature distribution to lower temperatures. In particular, it causes a longer left  
17 tail of the temperature distribution which extends down to 177 K (or 5 K colder than the  
18 temperature distribution based solely on  $T_{CHEM-CLIM}$ ).

19 The effect of the parameterisation on PSCs is investigated by evaluating the 30-year average  
20 difference in PSC surface area density between the perturbation and control simulations  
21 (perturbation minus control). PSC surface area density controls the amount of reactive  
22 chlorine species produced, which cause ozone destruction. Fig. 11 shows the difference in  
23 PSC surface area density at a height of 21 km for July. The perturbation run results in  
24 increases in surface area density for all PSCs (i.e. combined type I and II) of  $6-10 \mu\text{m}^2 \text{cm}^{-3}$   
25 over the Antarctic Peninsula and  $>10 \mu\text{m}^2 \text{cm}^{-3}$  over the Bellingshausen Sea. Relative to the  
26 control run, these are equivalent to increases of more than 50% over the northern tip of the  
27 Antarctic Peninsula, and at least 30% over the Bellingshausen Sea. The Weddell Sea region  
28 shows a non-significant decrease in PSC surface area density. This is not unexpected, even  
29 though the first order expectation is for a large-area increase in PSCs. The chemistry-climate  
30 model is interactive: Changing PSCs change chlorine activation, which impacts ozone loss.  
31 Changing ozone alters the heating rates that impact temperatures and circulation. What is  
32 diagnosed in Fig. 11 (and related figures) is the difference between two climate equilibrium

1 states for identical boundary conditions (compare e.g. Braesicke et al., 2013). Consequently,  
2 what is shown in the figures is locally strongly influenced by the additional parameterisation  
3 (adding localised cooling and thus producing more PSCs), but in regions away from the direct  
4 impact the response can be determined by feedback mechanisms. Fig. 11 additionally  
5 separates these differences into their individual contributions from type I and type II PSCs. It  
6 is type I (type II) PSCs which are largely responsible for the overall PSC increase over the  
7 Antarctic Peninsula (Bellingshausen Sea). Note that significant differences in PSC surface  
8 area density were also evident in June, but not in August and September (not shown).

9

## 10 **6 Summary and discussion**

11 This study demonstrates that: i) UM high-resolution (4 km) mesoscale model simulations are  
12 able to accurately simulate the large mountain wave-induced temperature fluctuations in the  
13 lower stratosphere associated with strong westerly or north-westerly flow over the Antarctic  
14 Peninsula, and ii) UM low-resolution ( $2.5^\circ \times 3.75^\circ$ ) climate model simulations are completely  
15 unable to resolve such temperature fluctuations. These fluctuations act as a significant source  
16 of localised PSC formation as they enable stratospheric temperatures which otherwise would  
17 remain above the temperature threshold for PSC formation, to fall below it. With low spatial  
18 resolution a model is unable to resolve such temperature fluctuations, and as a consequence  
19 underestimate mountain wave-induced PSCs and the attendant PSC-induced ozone depletion.  
20 This in turn is also a good rationale for using the negative temperature anomalies only for the  
21 call to the chemistry scheme. On a sub-grid scale going below a threshold temperature will  
22 produce additional PSCs, whereas staying above will not trigger PSCs. So for a grid-box  
23 averaged PSC coverage only additional incidents below the threshold temperature increase  
24 the coverage. Certainly for such an assumption to be true the sub-grid wave train should be  
25 slowly evolving horizontally compared to the model time step as to produce an additional  
26 PSC occurrence frequency on the fringes of the synoptic-scale threshold temperature regions,  
27 as has been illustrated with Fig. 9 and discussed above.

28 To investigate the impact of temperature fluctuations due to unresolved (sub-grid scale)  
29 mountain waves the parameterisation of Dean et al. (2007) was implemented in the UM  
30 climate model. It describes the vertical evolution of a linear hydrostatic wave forced by  
31 steady, stably stratified flow over a two-dimensional ridge. By determining the vertical  
32 evolution of the wave amplitude and the wave phase (alternative schemes such as Wells et al.

1 (2011) solely compute the wave amplitude), the parameterisation is able to calculate the  
2 maximum downward and upward vertical displacement and subsequently the associated  
3 positive and negative temperature fluctuations. Its performance was assessed against the  
4 mesoscale model simulations. This comparison demonstrated that: i) the parameterised  
5 temperature fluctuations lie within the spread of the mesoscale model response, and ii) the  
6 amplitude and phase of the parameterised temperature fluctuations are broadly in agreement  
7 with the mean mesoscale model response. However, the comparison also showed that the  
8 parameterisation cannot represent the upstream tilt of the phase lines with height, which is  
9 characteristic of a coherent hydrostatic mountain wave, due to it representing the Peninsula by  
10 a series of independent sub-grid scale ridges which each launch a mountain wave vertically  
11 through the column of air above. Moreover, the parameterisation also does not represent  
12 trapped mountain lee waves, which can result in localised cooling many hundreds of  
13 kilometres downstream (e.g. Dörnbrack et al., 1999).

14 The study followed this by assessing the impact on PSCs using the UKCA chemistry-climate  
15 model. It was found that adding the wave-induced cooling phase to the resolved temperature  
16 had a substantial impact on the frequency and magnitude of low temperatures which satisfy  
17 PSC thresholds, resulting in a regional 30-50% increase in PSC surface area density during  
18 July at a height of 21 km over the Antarctic Peninsula and the Bellingshausen Sea. It should  
19 be stressed that we were unable to compare these results with observations as: i) detailed  
20 measurements of Antarctic PSCs over a decadal time scale are not available at present (Austin  
21 et al., 2010), and ii) global atmospheric reanalyses do not resolve small-scale temperature  
22 fluctuations. Our decision to neglect the wave-induced warming phase might imply that the  
23 diagnosed increase should perhaps be considered as an upper bound. However, the formation  
24 of PSCs downstream due to trapped lee waves is currently not represented in the model.  
25 Carslaw et al. (1999) remedied this by applying a horizontal ‘influence function’ to simulate  
26 cooling downstream of orography, and a similar approach will be considered in future  
27 implementations of the scheme in UKCA chemistry-climate model. The simulation of PSC  
28 differences both upstream and downstream of the Antarctic Peninsula, and hence removed  
29 from the actual region where the parameterisation impacts temperatures directly, is suggestive  
30 of a new climate-equilibrium state being established in the model that allow non-local effects  
31 to occur. Investigation of this will be the subject of future study. Moreover, the  
32 parameterisation might offer a method for some models improving lower stratospheric  
33 temperatures that satisfy more often conditions for PSC formation, the failure of which was



1 suggested by Austin et al. (2010) to be one of the main reasons for the poor simulation of  
2 ozone depletion.

3 It is worth noting that other biases can affect the ability of chemistry-climate models to  
4 realistically simulate PSCs. For example, the failure of many models to represent the effects  
5 of non-orographic gravity wave drag can result in unrealistically cold temperatures in the  
6 Southern Hemisphere winter stratosphere (Orr et al., 2010), i.e. resulting in synoptic-scale  
7 temperatures which fall below the PSC temperature threshold when in reality they should be  
8 above it, which as a consequence cause the formation of too many PSCs and associated  
9 increased ozone losses (Austin et al., 2003). Moreover, the standard quasi-equilibrium PSC  
10 scheme used by the UKCA module does not advect PSC particles (Feng et al., 2011), i.e. the  
11 impact on PSC formation of the mountain wave parameterisation scheme is localised to  
12 wherever the temperature fluctuations are applied. This means that the occurrence of  
13 circumpolar belts of PSCs which have been attributed to mountain wave-induced PSCs over  
14 regions such as the Antarctic Peninsula would not be represented. However, future work will  
15 investigate replacing the quasi-equilibrium PSC scheme with the full microphysical scheme  
16 DLAPSE (Denitrification by Lagrangian Particle Sedimentation), which uses a Lagrangian  
17 trajectory scheme and as such is able to transport PSC particles away from the region of  
18 formation (Feng et al., 2011). However, the current study illustrates that a more  
19 comprehensive treatment of sub-grid scale mountain waves in a global climate model leads to  
20 realistic localised temperature change diagnostics. Subsequently, we have been able to assess  
21 and characterise the localised impact of the modelled temperature fluctuations in a  
22 comprehensive chemistry-climate model. Further work will investigate the non-localised  
23 effects in more detail.

24

## 25 **Acknowledgements**

26 The authors thank T. Phillips for providing much assistance in producing the figures. This  
27 study is part of the British Antarctic Survey Polar Science for Planet Earth Programme. It was  
28 funded by The Natural Environment Research Council (grant number NE/H022988/1). AIRS  
29 data are distributed by NASA Goddard Earth Science Data Information and Services Center.  
30 This work made use of the facilities HECToR, the UK's national high-performance  
31 computing service, which is provided by UoE HPCx Ltd at the University of Edinburgh, Cray

1 Inc and NAG Ltd, and funded by the Office of Science and Technology through EPSRC's  
2 High End Computing Programme.

3

#### 4 **References**

5 Alfred, J., Fromm, M., Bevilacqua, R., Nedoluha, G., Strawa, A., Poole, L., and Wickert, J.:  
6 Observation and analysis of polar stratospheric clouds detected by POAM III and SAGE III  
7 during the SOLVE II/VINTERSOL campaign in the 2002/2003 Northern Hemisphere winter,  
8 *Atmos. Chem. Phys.*, 7, 2151-2163, doi: 10.5194/acp-7-2151-2007, 2007.

9 Alexander, J. M., and Barnett C. D.: Using satellite observations to constrain gravity wave  
10 parameterizations for global models, *J. Atmos. Sci.*, 64, 1652–1665, doi: 10.1175/JAS3897.1,  
11 2007.

12 Alexander, J. M., and Teitelbaum, H.: Observation and analysis of a large amplitude  
13 mountain wave event over the Antarctic Peninsula, *J. Geophys. Res.*, 112, D21103, doi:  
14 10.1029/2006JD008368, 2007.

15 Alexander, S. P., Klekociuk, A. R., Pitts, M. C., McDonald, A. J., and Arevalo-Torres, A.:  
16 The effect of orographic gravity waves on Antarctic polar stratospheric cloud occurrence and  
17 composition, *J. Geophys. Res.*, 116, D06109, doi: 10.1029/2010JD015184, 2011.

18 Alexander, S. P., Klekociuk, A. R., McDonald, A. J., and Pitts, M. C.: Quantifying the role of  
19 orographic gravity waves on polar stratospheric cloud occurrence in the Antarctic and the  
20 Arctic, *J. Geophys. Res.*, 118, 11493-11507, doi: 10.1002/2013JD020122, 2013.

21 Aumann, H. H., et al.: AIRS/AMSU/HSB on the Aqua mission: Design, science objective,  
22 data products, and processing systems, *IEEE T. Geosci. Remote*, 41, 253–264, doi:  
23 10.1109/TGRS.2002.808356, 2003.

24 Austin, J., and Butchart, N.: Coupled chemistry-climate model simulations for the period  
25 1980 to 2020: Ozone depletion and the start of ozone recovery, *Q. J. Roy. Meteor. Soc.*, 129,  
26 3225-3249, doi: 10.1256/qj.02.203, 2003.

27 Austin, J., Struthers, H., Scinocca, J., Plummer, D. A., Akiyoshi, H., Baumgaertner, A. J. G.,  
28 Bekki, S., Bodeker, G. E., Braesicke, P., Brühl, C., Butchart, N., Chipperfield, M. P., Cugnet,  
29 D., Dameris, M., Dhomse, S., Frith, S., Garny, H., Gettelman, A., Hardiman, S. C., Jöckel, P.,  
30 Kinnison, D., Kubin, A., Lamarque, J. F., Langematz, U., Mancini, E., Marchand, M.,

1 Michou, M., Morgenstern, O., Nakamura, T., Nielsen, J. E., Pitari, G., Pyle, J., Rozanov, E.,  
2 Shepherd, T. G., Shibata, K., Smale, D., Teyssèdre, H., and Yamashita, Y.: Chemistry-climate  
3 model simulations of spring Antarctic ozone, *J. Geophys. Res.*, 115, D00M11, doi:  
4 10.1029/2009JD013577, 2010.

5 Braesicke, P., Keeble, J., Yang, X., Stiller, G., Kellmann, S., Abraham, N. L., Archibald, A.,  
6 Telford, P., and Pyle, J. A.: Circulation anomalies in the Southern Hemisphere and ozone  
7 changes, *Atmos. Chem. Phys.*, 13, 10677-10688, doi:10.5194/acp-13-10677-2013, 2013.

8 Campbell, J. R., and Sassen, K.: Polar stratospheric clouds at the South Pole from 5 years of  
9 continuous lidar data: Macrophysical, optical, and thermodynamic properties, *J. Geophys.*  
10 *Res.*, 113, D20204, doi: 10.1029/2007JD009680, 2008.

11 Cariolle, D., Muller, S., Cayla, F., and McCormick, M. P.: Mountain waves, polar  
12 stratospheric clouds, and ozone depletion over Antarctica, *J. Geophys. Res.*, 94, 11233-11240,  
13 doi: 10.1029/JD094iD09p11233, 1989.

14 Carslaw, K. S., Wirth, M., Tsias, A., Luo, B. P., Dörnbrack, A., Leutbecher, M., Volkert, H.,  
15 Renger, W., Bacmeister, J. T., and Peter, T.: Particle microphysics and chemistry in remotely  
16 observed mountain polar stratospheric clouds, *J. Geophys. Res.*, 103, 5785-5796, doi:  
17 10.1029/97JD03626, 1998a.

18 Carslaw, K. S., Wirth, M., Tsias, A., Luo, B. P., Dörnbrack, A., Leutbecher, M., Volkert, H.,  
19 Renger, W., Bacmeister, J. T., Reimer, E., and Peter, Th.: Increased stratospheric ozone  
20 depletion due to mountain-induced atmospheric waves, *Nature*, 391, 675-678, 1998b.

21 Carslaw, K. S., Peter, T., Bacmeister, J. T., and Eckermann, S. D.: Widespread solid particle  
22 formation by mountain waves in the Arctic stratosphere, *J. Geophys. Res.*, 104, 1827-1836,  
23 doi: 10.1029/1998JD100033, 1999.

24 Dean, S. M., Flowerdew, J., Lawrence, B. N., and Eckermann, S. D.: Parameterisation of  
25 orographic cloud dynamics in a GCM, *Clim. Dynam.*, 28, 581-597, doi: 10.1007/s00382-006-  
26 0202-0, 2007.

27 Donlon, C. J., Martin, M., Stark, J. D., Roberts-Jones, J., Fiedler, E., and Wimmer, W.: The  
28 Operational Sea Surface Temperature and Sea Ice analysis (OSTIA), *Remote Sensing of the*  
29 *Environment*, 116, 140-158, doi: 10.1016/j.rse.2010.10.017, 2011.

1 Dörnbrack, A., Leutbecher, M., Kivi, R., and Kyrö, E.: Mountain-wave-induced record low  
2 stratospheric temperatures above northern Scandinavia, *Tellus*, 51A, 951-963, 1999.

3 Dörnbrack, A., and Leutbecher, M.: Relevance of mountain waves for the formation of polar  
4 stratospheric clouds over Scandinavia: A 20 year climatology, *J. Geophys. Res.*, 106, 1583-  
5 1593, doi: 10.1029/2000JD900250, 2001.

6 Dörnbrack, A., Birner, T., Fix, A., Flentje, H., Meister, A., Schmid, H., Browell, E. V., and  
7 Mahoney, M. J.: Evidence for inertia gravity waves forming in polar stratospheric clouds over  
8 Scandinavia, *J. Geophys. Res.*, 107, 8287, doi: 10.1029/2001JD000452, 2002.

9 Dörnbrack, A., Pitts, M. C., Poole, L. R., Orsolini, Y. J., Nishii, K., and Nakamura, H.: The  
10 2009-2010 Arctic stratospheric winter – general evolution, mountain waves and predictability  
11 of an operational weather forecast model, *Atmos. Chem. Phys.*, 12, 3659-3675, doi:  
12 10.5194/acp-12-3659-2012, 2012.

13 Eckermann, S. D., Hoffmann, L., Höpfner, M., Wu, D. L., and Alexander, M. J.: Antarctic  
14 NAT PSC belt of June 2003: Observational validation of the mountain wave seeding  
15 hypothesis, *Geophys. Res. Lett.*, 36, L02807, doi: 10.1029/2008GL036629, 2009.

16 Eyring, V., Butchart, N., Waugh, D. W., Akiyoshi, H., Austin, J., Bekki, S., Bodeker, G. E.,  
17 Boville, B. A., Brühl, C., Chipperfield, M. P., Cordero, E., Dameris, M., Deushi, M., Fioletov,  
18 V. E., Frith, S. M., Garcia, R. R., Gettelman, A., Giorgetta, M. A., Grewe, V., Jourdain, L.,  
19 Kinnison, D. E., Mancini, E., Manzini, E., Marchand, M., Marsh, D. R., Nagashima, T.,  
20 Newman, P. A., Nielsen, J. E., Pawson, S., Pitari, G., Plummer, D. A., Rozanov, E., Schraner,  
21 M., Shepherd, T. G., Shibata, K., Stolarski, R. S., Struthers, H., Tian, W., and Yoshiki, M.:  
22 Assessment of temperature, trace species and ozone in chemistry-climate model simulations  
23 of the recent past, *J. Geophys. Res.*, 111, D22308, doi: 10.1029/2006JD007327, 2006.

24 Eyring, V., Arblaster, J. M., Cionni, I., Sedláček, J., Perlwitz, J., Young, P. J., Bekki, S.,  
25 Bergmann, D., Cameron-Smith, P., Collins, W. J., Faluvegi, G., Gottschaldt, K.-D., Horowitz,  
26 L. W., Kinnison, D. E., Lamarque, J.-F., Marsh, D. R., Saint-Martin, D., Shindell, D. T.,  
27 Sudo, K., Szopa, S., and Watanabe, S.: Long-term ozone changes and associated climate  
28 impacts in CMIP5 simulations, *J. Geophys. Res.*, 118, doi: 10.1002/jgrd.50316.

29 Feng, W., Chipperfield, M. P., Davies, S., Mann, G. W., Carslaw, K. S., Dhomse, S., Harvey,  
30 L., Randall, C., and Santee, M. L.: Modelling the effect of denitrification on polar ozone

1 depletion for Arctic winter 2004/2005, *Atmos. Chem. Phys.*, 11, 6559-6573, doi:  
2 10.5194/acp-11-6559-2011, 2011.

3 Grimsdell, A. W., Alexander, M. J., May, P. T., and Hoffmann, L.: Model study of waves  
4 generated by convection with direct validation via satellite, *J. Atmos. Sci.*, 67, 1617–1631,  
5 doi: 10.1175/2009JAS3197.1, 2010.

6 Hewitt, H. T., Copsey, D., Culverwell, I. D., Harris, C. M., Hill, R. S. R., Keen, A. B.,  
7 McLaren, A. J., and Hunke, E. C.: Design and implementation of the infrastructure of  
8 HadGEM3: the next-generation Met Office climate modelling system, *Geoscientific Model  
9 Development*, 4, 223-253, doi: 10.5194/gmd-4-223-2011, 2011.

10 Hoffmann, L., and Alexander, M. J.: Retrieval of stratospheric temperatures from  
11 Atmospheric Infrared Sounder radiance measurements for gravity wave studies, *J. Geophys.  
12 Res.*, 114, D07105, doi: 10.1029/2008JD011241, 2009.

13 Hoffmann, L., and Alexander, M. J.: Occurrence frequency of convective gravity waves  
14 during the North American thunderstorm season, *J. Geophys. Res.*, 115, D20111, doi:  
15 10.1029/2010JD014401, 2010.

16 Hoffmann, L., Xue, X., and Alexander, M. J.: A global view of stratospheric gravity wave  
17 hotspots located with Atmospheric Infrared Sounder observations, *J. Geophys. Res.*, 118,  
18 416-434, doi: 10.1029/2012JD018658, 2013.

19 Höpfner, M., Larsen, N., Spang, R., Luo, B. P., Ma, J., Svendsen, S. H., Eckermann, S. D.,  
20 Knudsen, B., Massoli, P., Cairo, F., Stiller, G., Clarmann, T. v., and Fischer, H.: MIPAS  
21 detects Antarctic stratospheric belt of NAT PSCs caused by mountain waves, *Atmos. Chem.  
22 Phys.*, 6, 1221-1230, doi: 10.5194/acp-6-1221-2006, 2006.

23 Jensen, E. J., Toon, O., Tabazadeh, A., and Drdla, K.: Impact of polar stratospheric cloud  
24 particle composition, number density, and lifetime on denitrification, *J. Geophys. Res.*, 107,  
25 8284, doi: 10.1029/2001JD000440, 2002.

26 Liu, H., Jezek, K., Li, B., Zhao, Z.: Radarsat Antarctic Mapping Project digital elevation  
27 model version 2, National Snow and Ice Data Center, Boulder, Colorado, 2001.

28 Lott, F., Miller, M.: A new subgrid scale orographic drag parameterization; its testing in the  
29 ECMWF model, *Q. J. Roy. Meteor. Soc.*, 123, 1010127, 1997.

1 Noel, V., Hertzog, A., and Chepfer, H.: CALIPSO observations of wave-induced PSCs with  
2 near-unity optical depth over Antarctica in 2006-2007, *J. Geophys. Res.*, 114, D05202, doi:  
3 10.1029/2008JD010604, 2009.

4 Noel, V., and Pitts, M.: Gravity wave events from mesoscale simulations, compared to polar  
5 stratospheric clouds observed from spaceborne lidar over the Antarctic Peninsula, *J. Geophys.*  
6 *Res.*, 117, D11207, doi: 10.1029/2011JD017318, 2012.

7 McDonald, A. J., George, S. E., and Woollands, R. M.: Can gravity waves significantly  
8 impact PSC occurrence in the Antarctic?, *Atmos. Chem. Phys.*, 9, 8825-8840, doi:  
9 10.5194/acp-9-8825-2009, 2009.

10 McFarlane, N. A.: The effect of orographically excited gravity wave drag on the general  
11 circulation of the lower stratosphere and troposphere, *J. Atmos. Sci.*, 44, 1775-1800, doi:  
12 10.1175/1520-0469(1987)044<1775:TEOOEG>2.0.CO;2, 1987.

13 Morgenstern, O., Braesicke, P., O'Connor, F. M., Bushell, A. C., Johnson, C. E., Osprey, S.  
14 M., and Pyle, J. A.: Evaluation of the new UKCA climate-composition model – Part I: The  
15 stratosphere, *Geoscientific Model Development*, 2, 43-57, doi: 10.5194/gmd-2-43-2009,  
16 2009.

17 Morgenstern, O., Giorgetta, M. K., Shibata, K., Eyring, V., Waugh, D. W., Shepherd, T. G.,  
18 Akiyoshi, H., Austin, J., Baumgaertner, A. J. G., Bekki, S., Braesicke, P., Brühl, C.,  
19 Chipperfield, M. P., Cugnet, D., Dameris, M., Dhomse, S., Frith, S. M., Garny, H.,  
20 Gettelman, S., Hardiman, S. C., Hegglin, M. I., Jöckel, P., Kinnison, D. E., Lamarque, J.-F.,  
21 Mancini, E., Manzini, E., Marchand, M., Michou, M., Nakamura, T., Nielsen, J. E., Olivié,  
22 D., Pitari, G., Plummer, D. A., Rozanov, E., Scinocca, J. F., Smale, D., Teyssèdre, H.,  
23 Toohey, M., Tian W., and Yamashita, Y.: Review of the formulation of present-generation  
24 stratospheric chemistry-climate models and associated external forcings, *J. Geophys. Res.*,  
25 115, D00M02, doi:10.1029/2009JD013728, 2010.

26 Orr, A., Marshall, G., Hunt, J. C. R., Sommeria, J., Wang, C., van Lipzig, N., Cresswell, D.,  
27 and King, J. C.: Characteristics of airflow over the Antarctic Peninsula and its response to  
28 recent strengthening of westerly circumpolar winds, *J. Atmos. Sci.*, 65, 1396-1413, doi:  
29 10.1175/2007JAS2498.1, 2008.

1 Orr, A., Bechtold, P., Scinocca, J., Ern, M., and Janiskova, M.: Improved middle atmosphere  
2 climate and forecasts in the ECMWF model through a nonorographic gravity wave drag  
3 parameterization, *J. Climate*, 5905-5926, doi: 10.1175/2010JCLI3490.1, 2010.

4 Orr, A., Bracegirdle T. J., Hoskings, J. S., Jung, T., Haigh, J. D., Phillips, T., and Feng, W.:  
5 Possible dynamical mechanisms for Southern Hemisphere climate change due to the ozone  
6 hole, *J. Atmos. Sci.*, 69, 2917-2932, doi: 10.1175/JAS-D-11-0210.1, 2012.

7 Orr, A., Phillips, T., Webster, S., Elvidge, A., Weeks, M., Hosking, J. S., and Turner, J.: Met  
8 Office Unified Model high resolution simulations of a strong wind event in Antarctica, *Q. J.*  
9 *Roy. Meteor. Soc.*, doi: 10.1002/qj.2296, 2014.

10 Pawson, S., Naujokat, B., and Labitzke, K.: On the polar stratospheric cloud formation  
11 potential of the northern stratosphere, *J. Geophys. Res.*, 100, 23215-23225, doi:  
12 10.1029/95JD01918, 1995.

13 Plougonven, R., Hertzog, A., and Teitelbaum, H.: Observations and simulations of large-  
14 amplitude mountain wave breaking over the Antarctic Peninsula, *J. Geophys. Res.*, 113,  
15 D16113, doi: 10.1029/2007JD009739, 2008.

16 Plougonven, R., Arsac, A., Hertzog, A., Guez, L., and Vial, F.: Sensitivity study for  
17 mesoscale simulations of gravity waves above Antarctica during Vorcore, *Q. J. Roy. Meteor.*  
18 *Soc.*, 136, 1371-1377, doi: 10.1002/qj.639, 2010.

19 Polvani, L. M., Previdi, M., and Deser, C.: Large cancellation, due to ozone recovery, of  
20 future Southern Hemisphere atmospheric circulation trends, *Geophys. Res. Lett.*, 38, doi:  
21 10.1029/2011GL046712, 2011.

22 Reinecke, P., and Durran, D. R.: The over-amplification of gravity waves in numerical  
23 solutions to flow over topography, *Mon. Weather Rev.*, 137, 1533-1549, doi:  
24 10.1175/2008MWR2630.1, 2009.

25 Solomon, S.: Stratospheric ozone depletion: A review of concepts and history, *Rev. Geophys.*,  
26 37, 3, 275-316, doi: 10.1029/1999RG000008, 1999.

27 SPARC Report N°6: Lifetimes of Stratospheric Ozone-Depleting Substances, Their  
28 Replacements, and Related Species, Edited by Ko, M. K. W., Newman P. A., Reimann, S.,  
29 and Strahan S. E., WCRP-15/2013, 2013.

- 1 Thompson, D. W. J., Solomon, S., Kushner, P. J., England, M. H., Grise, K. M., and Karoly,  
2 D. J.: Signatures of the Antarctic ozone hole in Southern Hemisphere surface climate change,  
3 Nature Geo., 4, 741-749, 2011.
- 4 Webster, S., Uddstrom, M., Oliver, H., and Vosper, S.: A high-resolution modelling case  
5 study of a severe weather event over New Zealand, Atmos. Sci. Lett., 9, 119-128, doi:  
6 10.1002/asl.172, 2008.
- 7 Wells, H., Vosper, S. B., and Yan, X.: An assessment of a mountain-wave parametrization  
8 scheme using satellite observations of stratospheric gravity waves, Q. J. Roy. Meteor. Soc.,  
9 137, 819-828, doi: 10.1002/qj.790, 2011.
- 10 Wu, D. L.: Mesoscale gravity wave variances from AMSU-A radiances, Geophys. Res. Lett.,  
11 31, L12114, doi: 10.1029/2004GL019562, 2004.
- 12 Wu, D. L., and Eckermann, S. D.: Global gravity wave variances from Aura MLS:  
13 Characteristics and interpretation, J. Atmos. Sci., 65, 3695-3718, doi:  
14 10.1175/2008JAS2489.1, 2008.
- 15



1 Table 1. Dates and times of the three mountain wave case studies for the AIRS measurements,  
 2 the start of the mesoscale and climate model simulations, and the model forecast/output  
 3 nearest the AIRS measurements (in UTC).

Case study	AIRS measurement	Model start	Model output time nearest the AIRS measurement
CS1	7 Aug 2011, 03:40	5 Aug 2011, 12:00	7 Aug 2011, 03:00 (T+39h)
CS2	2 Aug 2010, 18:59	1 Aug 2010, 00:00	2 Aug 2010, 19:00 (T+43h)
CS3	14 Jul 2010, 20:00	13 Jul 2010, 00:00	14 Jul 2010, 20:00 (T+44h)

4  
 5  
 6  
 7  
 8  
 9  
 10  
 11  
 12  
 13  
 14  
 15  
 16  
 17  
 18  
 19

## 1 **Figure captions**

2 Figure 1. The temperature weighting function (brightness temperature (K) / temperature (K))  
3 for the  $666.5\text{ cm}^{-1}$  AIRS channel. This function was calculated for a polar winter reference  
4 atmosphere, a 1 km altitude grid, and the nadir observation geometry.

5

6 Figure 2. Mesoscale model (left) and climate model (right) simulation of the 850 hPa wind  
7 field ( $\text{m s}^{-1}$ ) over the Antarctic Peninsula at the time of the CS1 (a, b), CS2 (c, d), and CS3 (e,  
8 f) mountain wave events. See Table 1 for dates. The black arrows are wind vectors (for the  
9 mesoscale model only 1 in every 40 grid points is shown). The colour shading indicates the  
10 wind magnitude. Also shown is the coastline of the Antarctic Peninsula.

11

12 Figure 3. Measured (left) and mesoscale model (right) estimates of brightness temperature  
13 perturbations (K) corresponding to the  $666.5\text{ cm}^{-1}$  AIRS channel at the time of the CS1 (top),  
14 CS2 (middle), and CS3 (bottom) mountain wave events. See Table 1 for dates. The  
15 horizontal black lines indicate the latitude band selected for a more detailed comparison,  
16 shown in Fig. 4. Also shown is the coastline of the Antarctic Peninsula.

17

18 Figure 4. Measured (gray) and mesoscale model simulated (blue) brightness temperature  
19 fluctuations (K) corresponding to the  $666.5\text{ cm}^{-1}$  AIRS channel along a latitude band  
20 intersecting the Antarctic Peninsula (indicated on Fig. 3) at the time of the CS1 (a), CS2 (b),  
21 and CS3 (c) mountain wave events. See Table 1 for dates. Model data have been re-sampled  
22 on the AIRS measurement grid. Note that the model domain does not always cover the full  
23 AIRS swath, therefore re-gridded model data are missing at some longitudes in CS1 and CS2.  
24 The solid lines show a  $1^\circ$  running mean in longitude of the individual temperature  
25 fluctuations.

26

27 Figure 5. Vertical profile of temperature fluctuations (K) resolved by the climate model  
28 (dashed line), resolved by the mesoscale model (stars and horizontal bars), and parameterised  
29 by the mountain wave scheme (solid line) at the time of the CS1 (a), CS2 (b), and CS3 (c)  
30 mountain wave events. See Table 1 for dates. The temperature fluctuations resolved by the

1 climate model and parameterised by the scheme are for the N48 grid box centered on  $-70^\circ$   
2 latitude and  $-63.75^\circ$  longitude, i.e. over the high-elevation ridge of the Antarctic Peninsula.  
3 The mesoscale model temperature fluctuations are the mean (stars) and spread ( $\pm$  two  
4 standard deviations, horizontal bars) of all the mesoscale model points within the same N48  
5 grid box.

6

7 Figure 6. Vertical cross section intersecting the Antarctic Peninsula along a latitude band at  $-$   
8  $70^\circ$  of the temperature fluctuation (K) simulated by the mesoscale model (left) and the  
9 mountain wave parameterisation (right) at the time of the CS3 mountain wave event. See  
10 Table 1 for dates. The grey shading indicates the height of the explicitly resolved orography.

11

12 Figure 7. Vertical profile of the wind speed  $U$  (resolved in the direction of the wave vector,  
13 which is taken to be the direction of the 850 hPa wind vector) simulated by the climate model  
14 (black line) and the mesoscale model (grey lines) at the time of the CS1 (a), CS2 (b), and CS3  
15 (c) mountain wave events. See Table 1 for dates. The climate model profile is from the same  
16 N48 grid box used for Fig. 5. The mesoscale model profiles are for all the mesoscale model  
17 points within the N48 grid box.

18

19 Figure 8. As Fig. 6, but for Brunt-Väisälä frequency  $N$  ( $s^{-1}$ ).

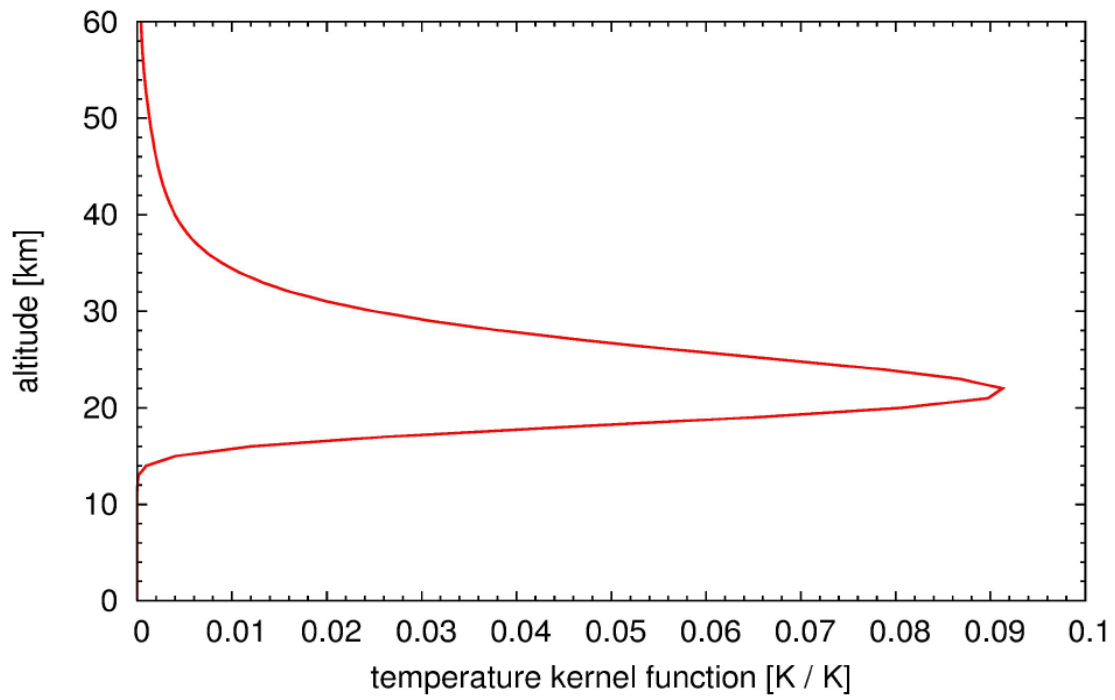
20

21 Figure 9. Impact of the mountain wave parameterisation during July at 21 km on the  
22 frequency  $f$  the 195 K (a) and 188 K (b) temperature thresholds are exceeded over the  
23 Antarctic Peninsula in the perturbation run of the chemistry-climate model. Shown are the  
24 30-year average percentage point difference between the frequency based on the explicitly  
25 resolved temperature  $T_{CHEM-CLIM}$  plus the parameterised temperature fluctuations  $\Delta T_{SSO}^-$ , and  
26 the frequency based solely on  $T_{CHEM-CLIM}$ , i.e.  $f_{T_{CHEM-CLIM} + \Delta T_{SSO}^-} - f_{T_{CHEM-CLIM}}$ . In the perturbed  
27 run,  $\Delta T_{SSO}$  is represented by the cooling phase only. The temperature thresholds of 195 and  
28 188 K are assumed to be representative of the formation of type I and II PSCs, respectively.  
29 Both differences are computed from 6-hourly fields. The contours indicate the 30-year  
30 average frequency  $f_{T_{CHEM-CLIM}}$ . Also shown is the coastline of the Antarctic Peninsula.

1  
2  
3  
4  
5  
6  
7  
8  
9  
10  
11  
12  
13  
14  
15  
16  
17  
18  
19  
20  
21  
22  
23  
24  
25  
26  
27

Figure 10: Impact of the mountain wave parameterisation during July at 21 km on the probability distributions of temperature over the Antarctic Peninsula in the perturbed run of the chemistry-climate model. Shown are the 30-year average temperature distributions based on the explicitly resolved temperature  $T_{CHEM-CLIM}$  plus the parameterised temperature fluctuations  $\Delta T_{SSO}^-$  (red colouring), and the frequency based solely on  $T_{CHEM-CLIM}$  (gray colouring). Regions where the two distributions overlap is coloured the darker shade of red. Both temperature distributions are for the N48 grid box as used in Figs. 5, 7 and 8. In the perturbed run,  $\Delta T_{SSO}^-$  is represented by the cooling phase only. The temperature thresholds of 195 and 188 K are marked as dashed vertical lines and are assumed to be representative of the formation of type Ia and II PSCs, respectively. Both temperature distributions are computed from 6-hourly fields.

Figure 11. Impact of the mountain wave parameterisation during July at 21 km on PSC surface area density ( $\mu\text{m}^2 \text{cm}^{-3}$ ) over the Antarctic Peninsula in the chemistry-climate model. The shading indicates the 30-year average difference in surface area density between the perturbation run and the control run (perturbation run minus the control run) for PSC types I and II (A), type I (B), and type II (C). The contours indicate the 30-year average PSC surface area density from the control run. Hatching denotes significance at the 95% confidence level using a two-tailed Student's T-Test. Also shown is the coastline of the Antarctic Peninsula.



1

2 Figure 1. The temperature weighting function (brightness temperature (K) / temperature (K))  
 3 for the 666.5 cm<sup>-1</sup> AIRS channel. This function was calculated for a polar winter reference  
 4 atmosphere, a 1 km altitude grid, and the nadir observation geometry.

5

6

7

8

9

10

11

12

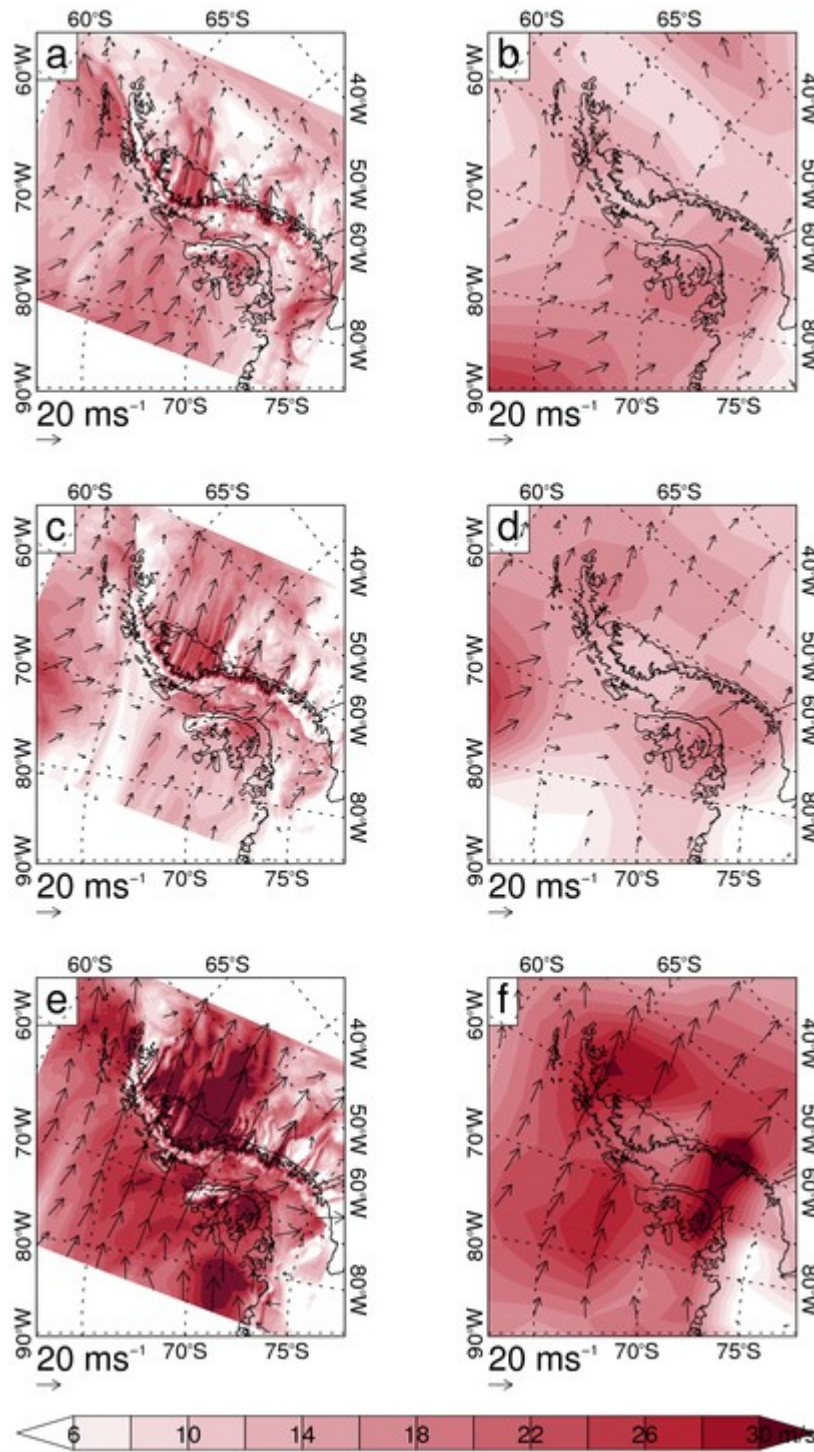
13

14

15

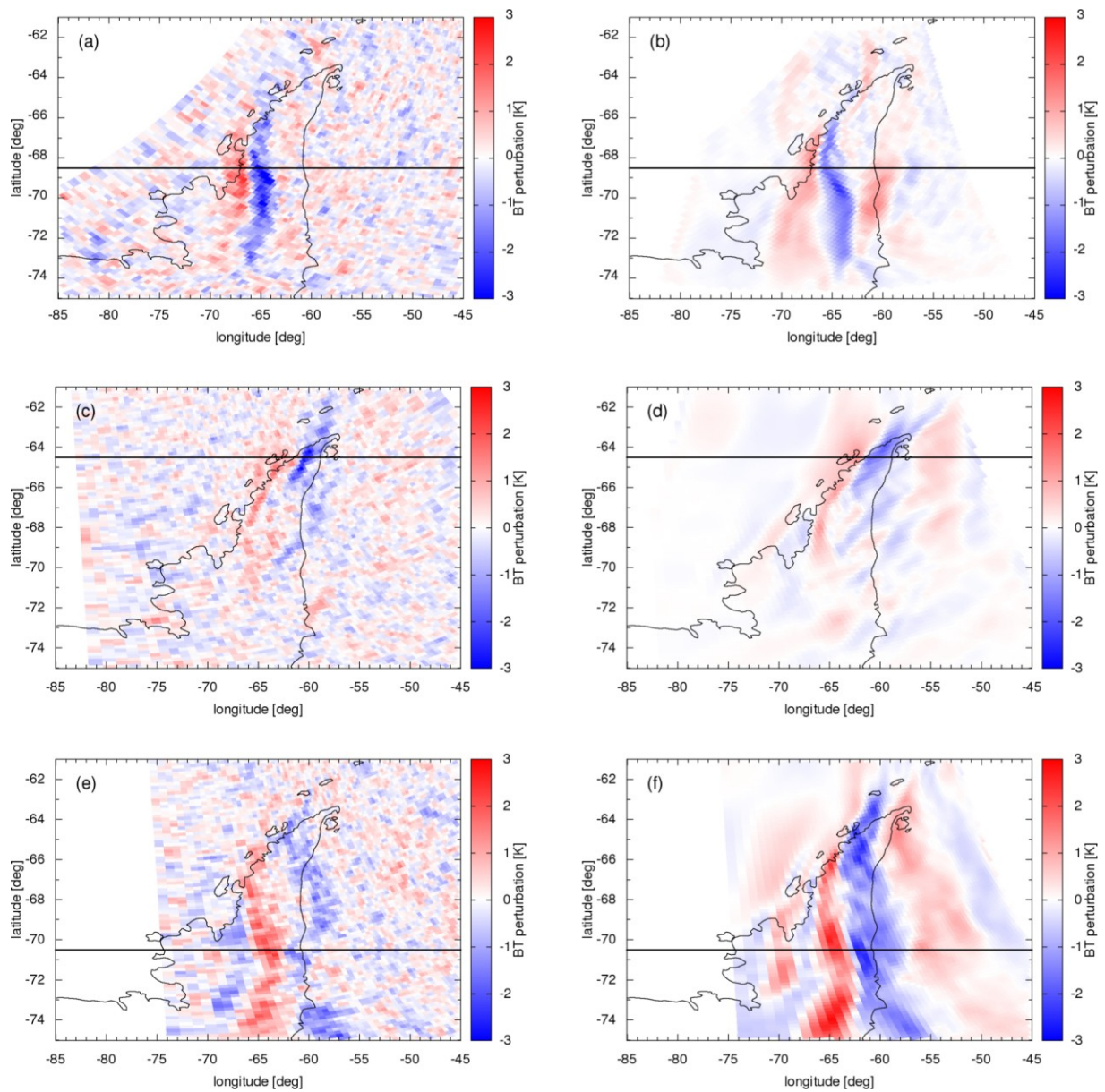
16

17



1

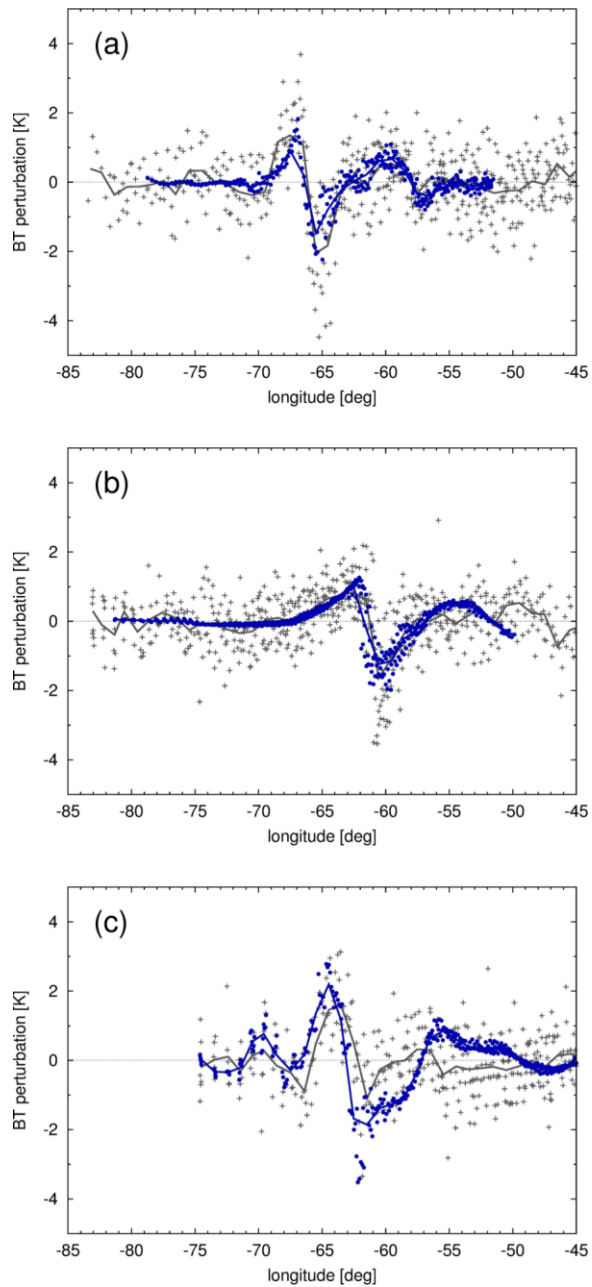
2 Figure 2. Mesoscale model (left) and climate model (right) simulation of the 850 hPa wind  
 3 field ( $\text{m s}^{-1}$ ) over the Antarctic Peninsula at the time of the CS1 (a, b), CS2 (c, d), and CS3 (e,  
 4 f) mountain wave events. See Table 1 for dates. The black arrows are wind vectors (for the  
 5 mesoscale model only 1 in every 40 grid points is shown). The colour shading indicates the  
 6 wind magnitude. Also shown is the coastline of the Antarctic Peninsula.



1  
 2 Figure 3. Measured (left) and mesoscale model (right) estimates of brightness temperature  
 3 perturbations (K) corresponding to the  $666.5\text{ cm}^{-1}$  AIRS channel at the time of the CS1 (top),  
 4 CS2 (middle), and CS3 (bottom) mountain wave events. See Table 1 for dates. The  
 5 horizontal black lines indicate the latitude band selected for a more detailed comparison,  
 6 shown in Fig. 4. Also shown is the coastline of the Antarctic Peninsula.

7  
 8  
 9



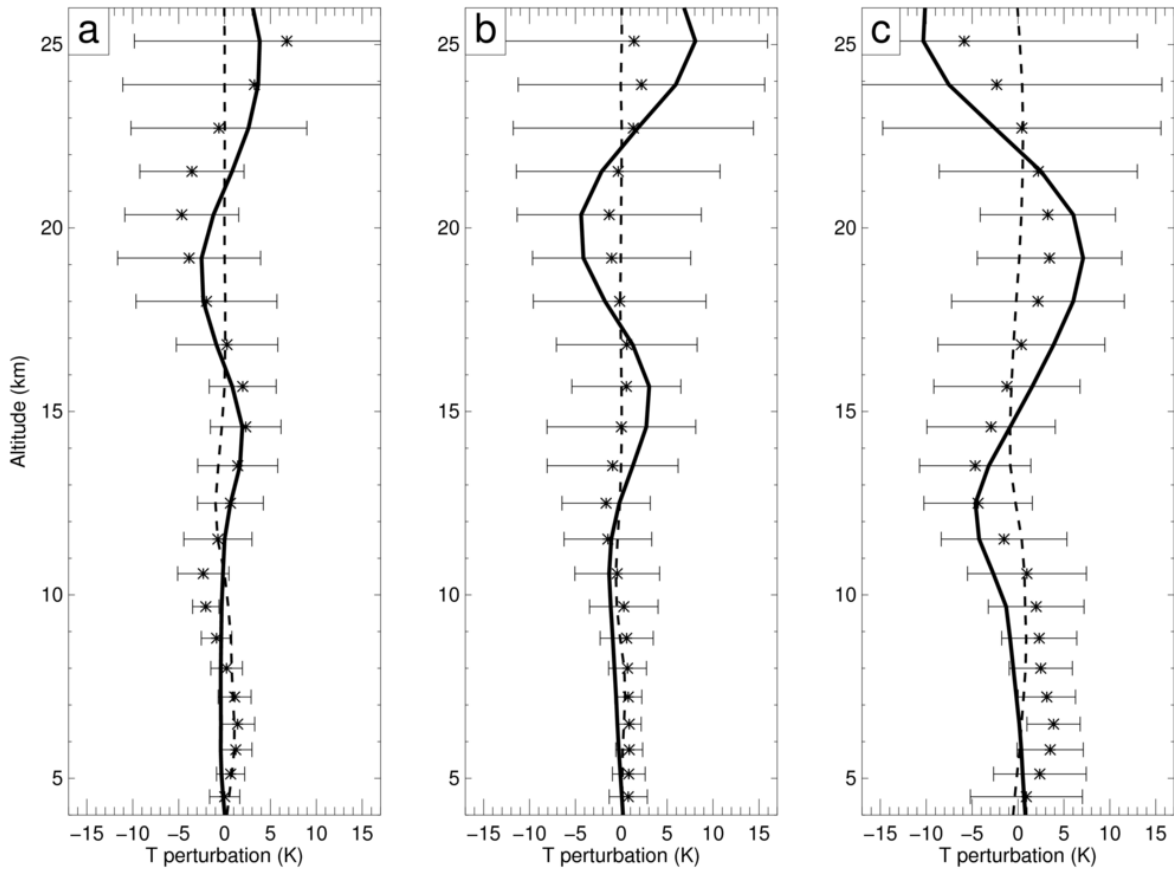


1

2 Figure 4. Measured (gray) and mesoscale model simulated (blue) brightness temperature  
 3 fluctuations (K) corresponding to the  $666.5 \text{ cm}^{-1}$  AIRS channel along a latitude band  
 4 intersecting the Antarctic Peninsula (indicated on Fig. 3) at the time of the CS1 (a), CS2 (b),  
 5 and CS3 (c) mountain wave events. See Table 1 for dates. Model data have been re-sampled  
 6 on the AIRS measurement grid. Note that the model domain does not always cover the full  
 7 AIRS swath, therefore re-gridded model data are missing at some longitudes in CS1 and CS2.  
 8 The solid lines show a  $1^\circ$  running mean in longitude of the individual temperature  
 9 fluctuations.

10





1

2 Figure 5. Vertical profile of temperature fluctuations (K) resolved by the climate model  
 3 (dashed line), resolved by the mesoscale model (stars and horizontal bars), and parameterised  
 4 by the mountain wave scheme (solid line) at the time of the CS1 (a), CS2 (b), and CS3 (c)  
 5 mountain wave events. See Table 1 for dates. The temperature fluctuations resolved by the  
 6 climate model and parameterised by the scheme are for the N48 grid box centered on  $-70^\circ$   
 7 latitude and  $-63.75^\circ$  longitude, i.e. over the high-elevation ridge of the Antarctic Peninsula.  
 8 The mesoscale model temperature fluctuations are the mean (stars) and spread ( $\pm$  two  
 9 standard deviations, horizontal bars) of all the mesoscale model points within the same N48  
 10 grid box.

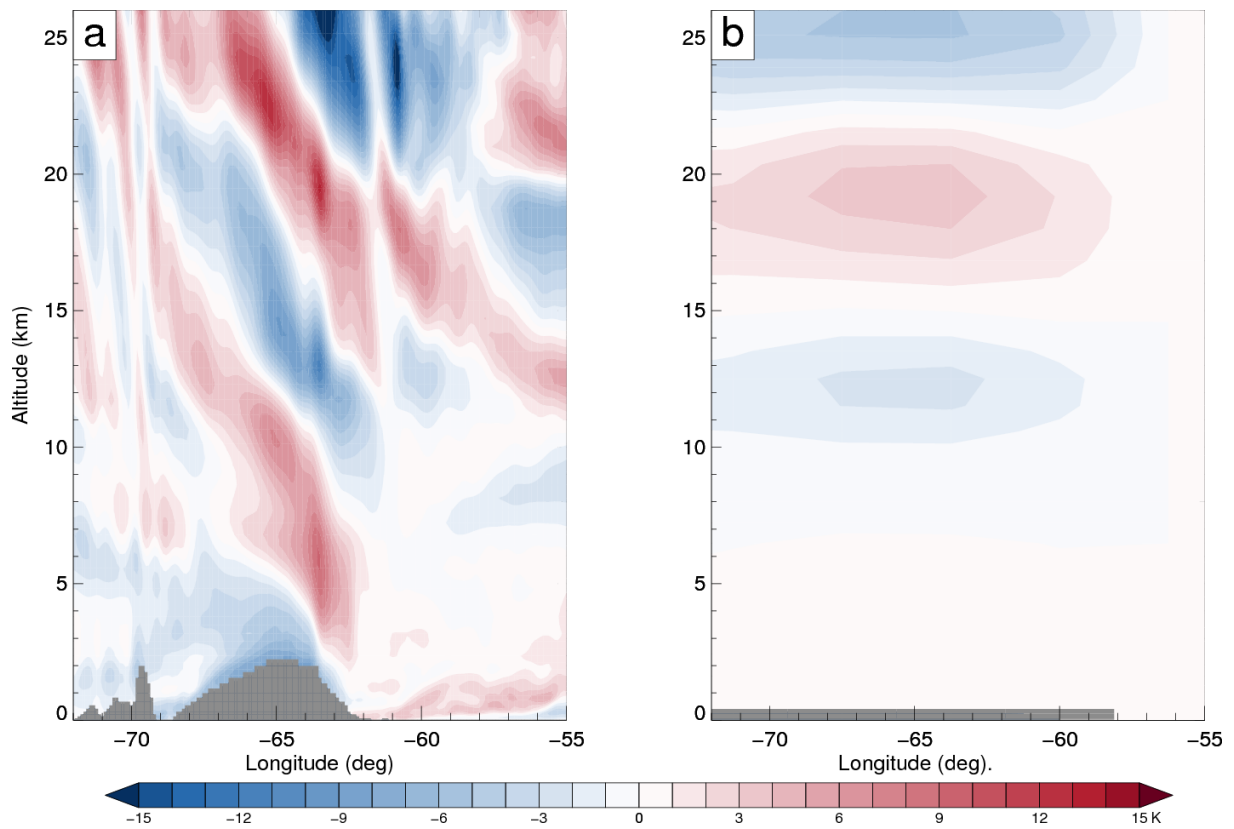
11

12

13

14

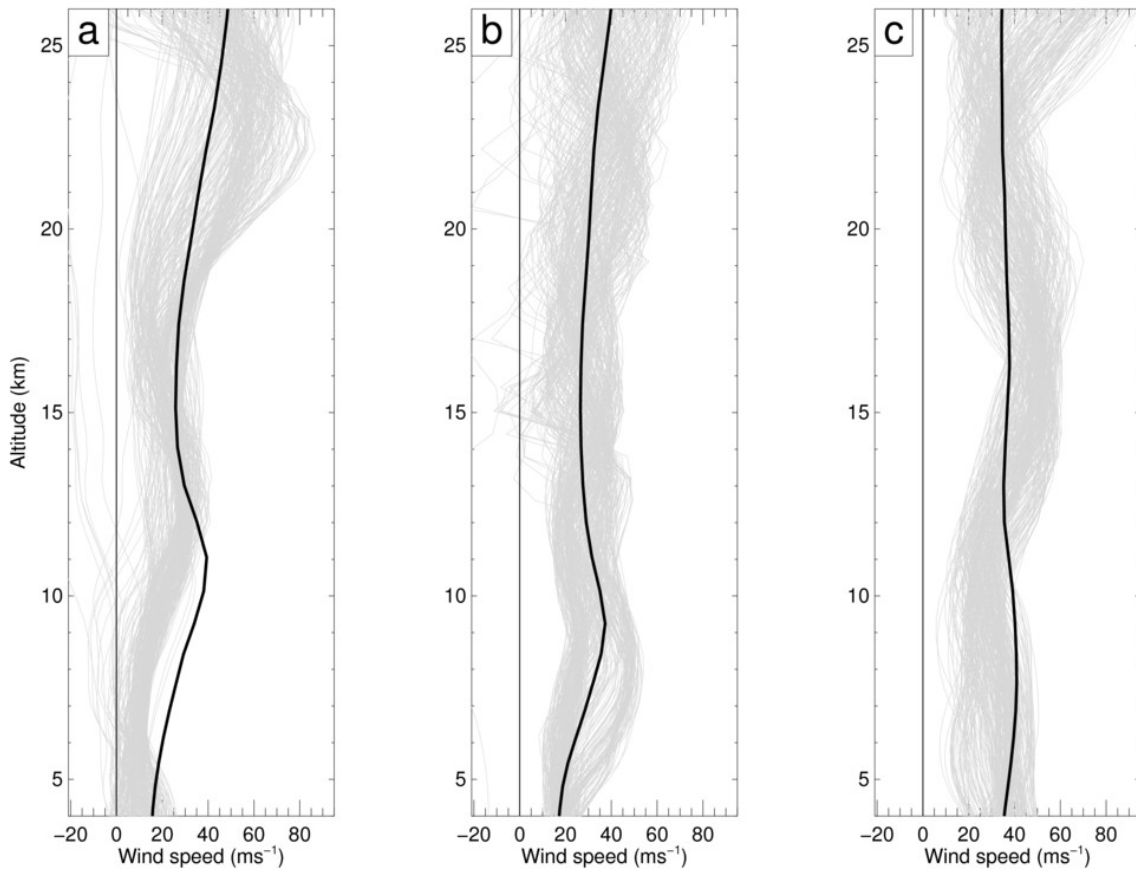
15



1

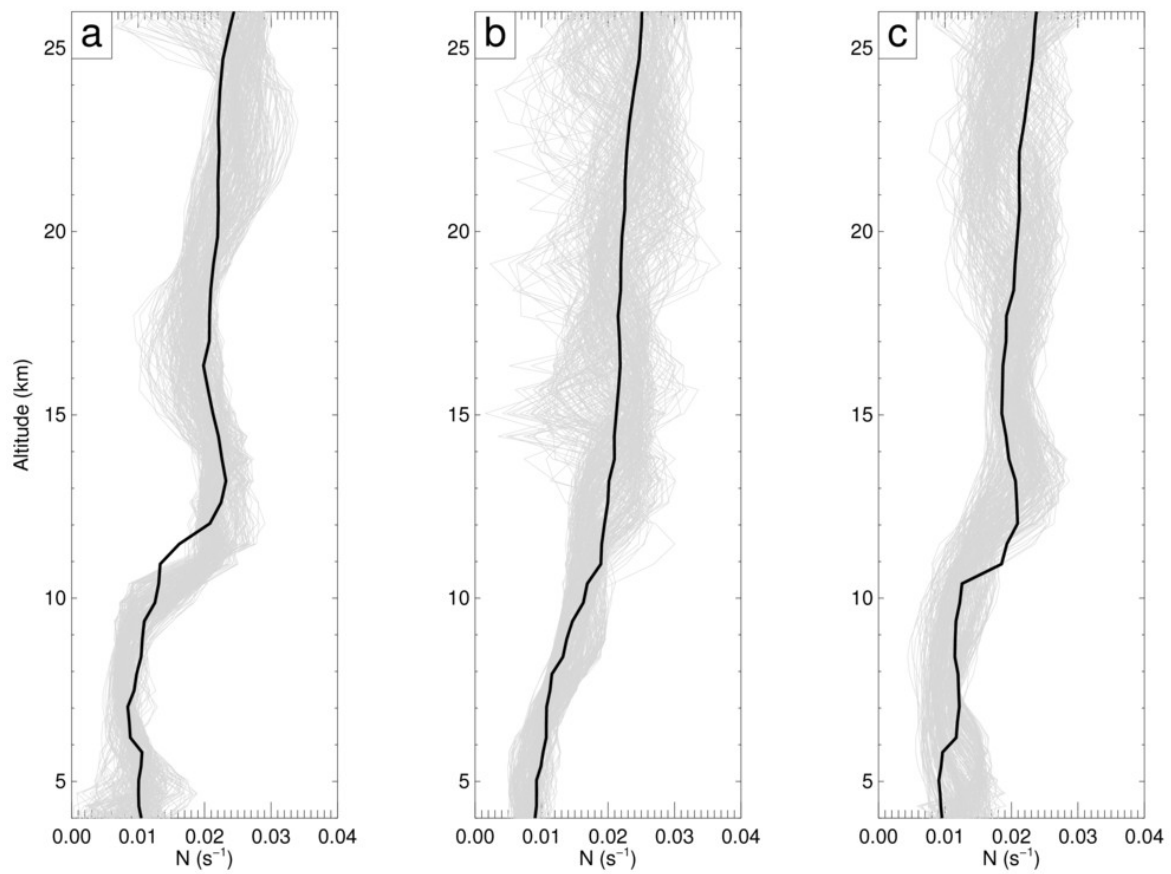
2 Figure 6. Vertical cross section intersecting the Antarctic Peninsula along a latitude band at -  
 3 70° of the temperature fluctuation (K) simulated by the mesoscale model (left) and the  
 4 mountain wave parameterisation (right) at the time of the CS3 mountain wave event. See  
 5 Table 1 for dates. The grey shading indicates the height of the explicitly resolved orography.

6



1  
 2 Figure 7. Vertical profile of the wind speed  $U$  (resolved in the direction of the wave vector,  
 3 which is taken to be the direction of the 850 hPa wind vector) simulated by the climate model  
 4 (black line) and the mesoscale model (grey lines) at the time of the CS1 (a), CS2 (b), and CS3  
 5 (c) mountain wave events. See Table 1 for dates. The climate model profile is from the same  
 6 N48 grid box used for Fig. 5. The mesoscale model profiles are for all the mesoscale model  
 7 points within the N48 grid box.

8  
 9  
 10  
 11  
 12  
 13  
 14  
 15



1

2 Figure 8. As Fig. 6, but for Brunt-Väisälä frequency  $N$  ( $\text{s}^{-1}$ ).

3

4

5

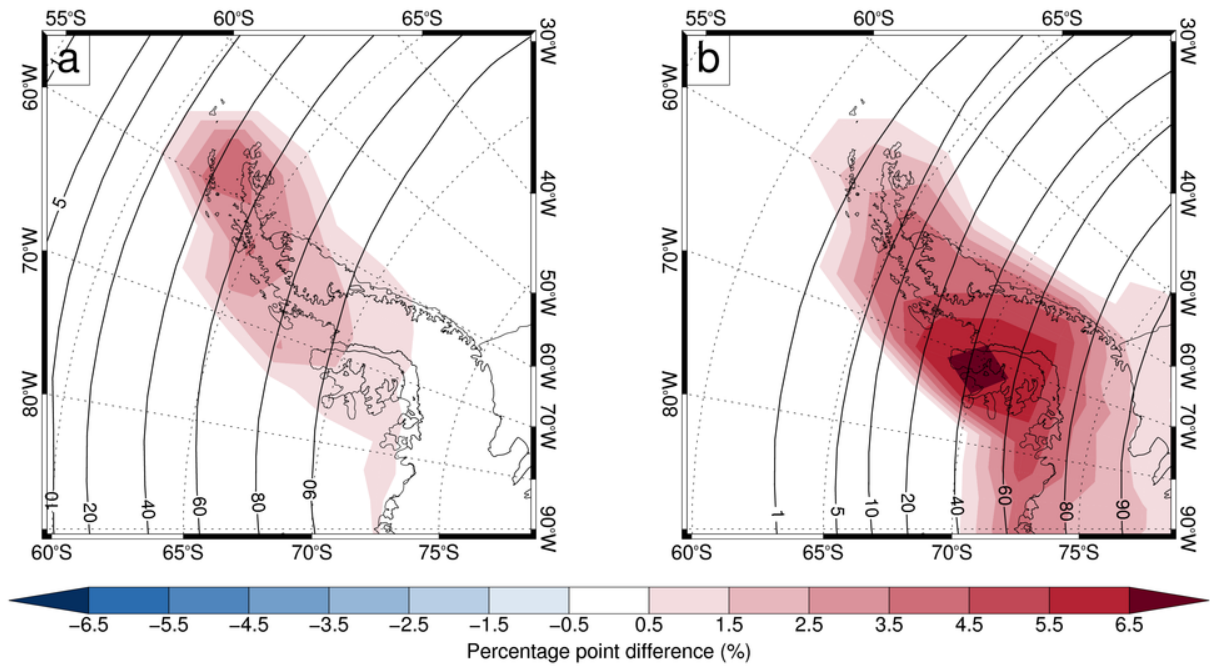
6

7

8

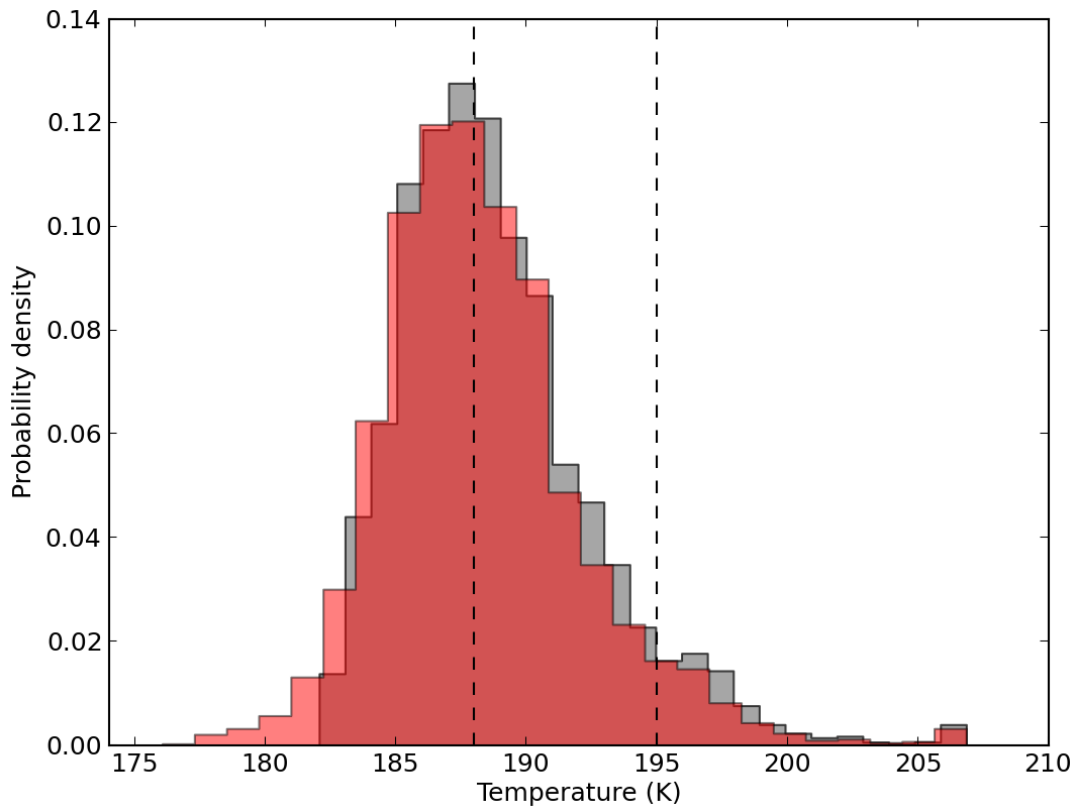
9

10



1  
 2 Figure 9. Impact of the mountain wave parameterisation during July at 21 km on the  
 3 frequency  $f$  the 195 K (a) and 188 K (b) temperature thresholds are exceeded over the  
 4 Antarctic Peninsula in the perturbation run of the chemistry-climate model. Shown are the  
 5 30-year average percentage point difference between the frequency based on the explicitly  
 6 resolved temperature  $T_{CHEM-CLIM}$  plus the parameterised temperature fluctuations  $\Delta T_{SSO}^-$ , and  
 7 the frequency based solely on  $T_{CHEM-CLIM}$ , i.e.  $f_{T_{CHEM-CLIM} + \Delta T_{SSO}^-} - f_{T_{CHEM-CLIM}}$ . In the perturbed  
 8 run,  $\Delta T_{SSO}$  is represented by the cooling phase only. The temperature thresholds of 195 and  
 9 188 K are assumed to be representative of the formation of type I and II PSCs, respectively.  
 10 Both differences are computed from 6-hourly fields. The contours indicate the 30-year  
 11 average frequency  $f_{T_{CHEM-CLIM}}$ . Also shown is the coastline of the Antarctic Peninsula.

12  
 13  
 14  
 15  
 16  
 17  
 18

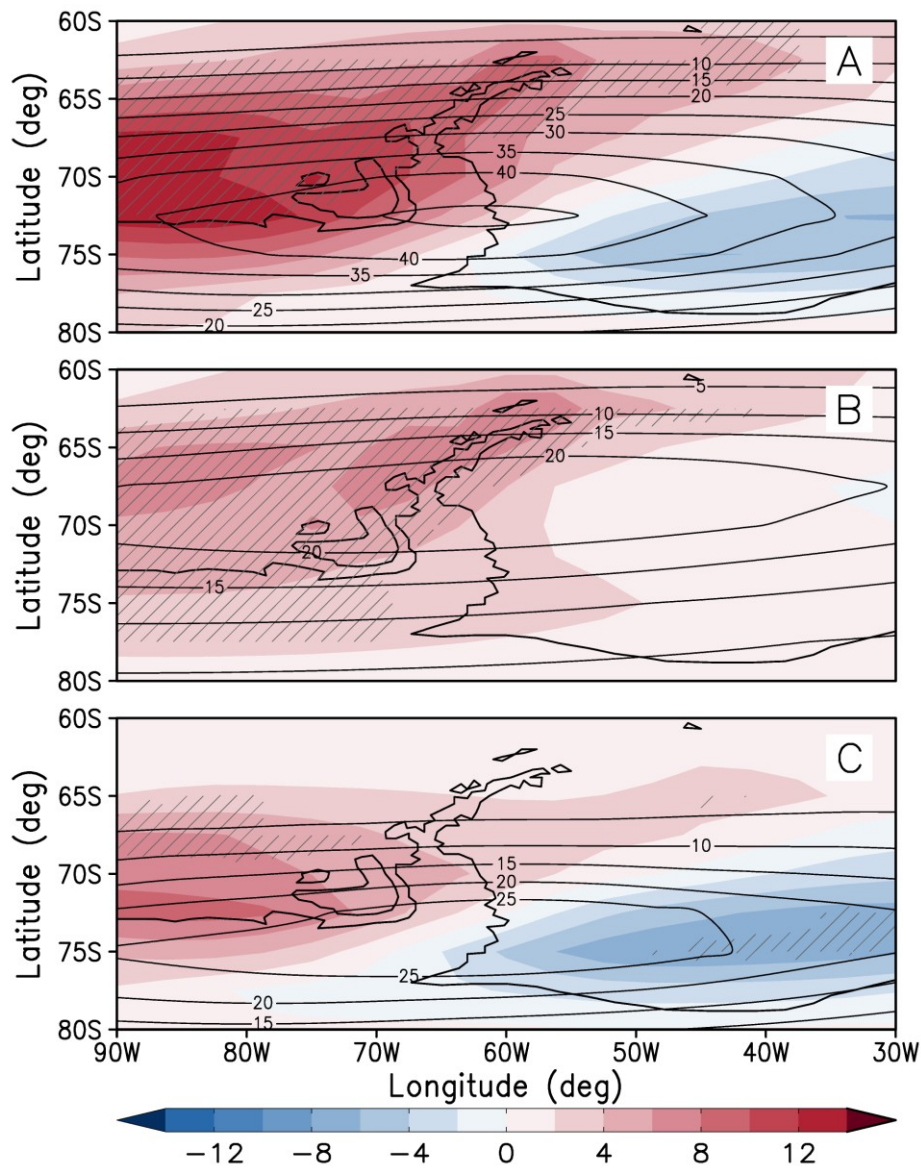


1

2 Figure 10: Impact of the mountain wave parameterisation during July at 21 km on the  
 3 probability distributions of temperature over the Antarctic Peninsula in the perturbed run of  
 4 the chemistry-climate model. Shown are the 30-year average temperature distributions based  
 5 on the explicitly resolved temperature  $T_{CHEM-CLIM}$  plus the parameterised temperature  
 6 fluctuations  $\Delta T_{SSO}^-$  (red colouring), and the frequency based solely on  $T_{CHEM-CLIM}$  (gray  
 7 colouring). Regions where the two distributions overlap is coloured the darker shade of red.  
 8 Both temperature distributions are for the N48 grid box as used in Figs. 5, 7 and 8. In the  
 9 perturbed run,  $\Delta T_{SSO}^-$  is represented by the cooling phase only. The temperature thresholds of  
 10 195 and 188 K are marked as dashed vertical lines and are assumed to be representative of the  
 11 formation of type Ia and II PSCs, respectively. Both temperature distributions are computed  
 12 from 6-hourly fields.

13

14



1  
 2 Figure 11. Impact of the mountain wave parameterisation during July at 21 km on PSC  
 3 surface area density ( $\mu\text{m}^2 \text{cm}^{-3}$ ) over the Antarctic Peninsula in the chemistry-climate model.  
 4 The shading indicates the 30-year average difference in surface area density between the  
 5 perturbation run and the control run (perturbation run minus the control run) for PSC types I  
 6 and II (A), type I (B), and type II (C). The contours indicate the 30-year average PSC surface  
 7 area density from the control run. Hatching denotes significance at the 95% confidence level  
 8 using a two-tailed Student's T-Test. Also shown is the coastline of the Antarctic Peninsula.